Quantum State Transfer: Protocols via Spin Chain Optimization and Construction

Chad Christian Nelmes

Master of Science by Research

University of York

Physics, Engineering and Technology

September, 2024

Abstract

Extensive research has outlined the pivotal role of appropriate spectra in enabling quantum information transfer via spin chain mirror inversion. Through a combination of numerical and analytical methods, researchers have identified configurations of nearest-neighbor couplings and on-site energies that facilitate perfect or near-perfect state transfer (PST-PGST). One notably effective model, derived from an equidistant spectrum (Christandl et al.), relies on strongly inhomogeneous couplings across the sites while leaving local magnetic fields unaltered. Through the use of evolutionary numerical methods, specifically a tailored genetic algorithm, we have uncovered an alternative spectrum. This alternative spectrum yields high-fidelity transfer solely through modulation of on-site energies. This spectrum, up to an approximate number of sites, allows for complete homogeneity of the couplings, thereby simplifying experimental requirements.

We've also used a secondary numerical approach in an inverse eigenvalue method to provide an auxiliary analysis in distinguishing quasi-perfect state transfer (QPST) and PST, as well as highlighting the trade-offs for both. Through these analyses we may propose alternative prescriptions which offers potential advantages for experimental implementation while still aiming for perfect or near-perfect state transfer.

Acknowledgements

"I will work my very hardest,
until they throw me out.
So that *when* they throw me out,
I won't have a guilty conscience."

- Jocelyn Bell Burnell

If not for Peter Nelmes, I would not have been able to be here and do any of this. My family is more than enough of an incentive for me to relentlessly try to do much more. My supervisors, Irene and Tim, have been nothing but gracious, hospitable and fantastic throughout (I believe to be) a very exciting and surprising 6 months in Yorkshire. I'm grateful for every second of it and eager to get started on some of the new areas of research!

Chad Christian Nelmes,
September, 2024.

Declaration of Authorship

I, ***Chad Christian Nelmes***, declare that this thesis titled, ***'Quantum State Transfer: Protocols via Spin Chain Optimization and Construction'*** and the work presented in it are my own.

- I declare that this thesis is a presentation of original work and I am the sole author. This work has not previously been presented for an award at this, or any other, University. All sources are acknowledged as References.

- Chapters 4 and 5 are based on the following (preprint) journal paper.

> **Fateh Bezaz, Chad C. Nelmes, Marta P. Estarellas, Timothy P. Spiller, Irene D'Amico**. 'Quasi-Perfect State Transfer in Spin Chains via the Parametrization of the On-Site Energies.' Preprint to be submitted to *Physica Scripta* (2024).

Contents

List of Tables

List of Figures

1

Introduction

'I have trouble with Dirac. This balancing on the dizzying path between genius and madness is awful.'

– Albert Einstein, Letter to
Paul Ehrenfest, Aug. 23, 1926.

Nature seems to be fundamentally quantum. How else could we have built technologies which were reliant on quantum mechanics providing novel insight? Quantum information science, the marriage between the principles of quantum mechanics and information theory, as a field, has seen exponential growth within the last few decades. The analysis of how might the underlying properties of quantum systems be understood in terms of facilitating the storage, processing and transmission of data has served as the basis of research concerning Quantum Information Processing (QIP). Subsequent investigations into how these properties might also be exploited for future technological advancement have served as the seminal motivation for the origin of one of the most recent technological divisions, the quantum technologies sector.

Historical technological triumphs, which require quantum theory to understand their underlying mechanisms, include (non-exhaustively) nuclear power, laser technology, medical imaging techniques, and solid-state electronics. New developments within this aforementioned division of quantum technologies, which instead now require the manipulation of quantum information for their successful application, include implementations for quantum sensing [1, 2, 3], quantum metrology [4, 5], and quantum communications (QKD) [6, 7], to name a few broad subdivisions. The rapid advancement of these technologies has not gone without notice, particularly regarding their potential benefits for the financial sector, government bodies, military operations, and even agricultural and environmental concerns, in countries where investment has been consistent [8, 9, 10, 11, 12, 13].

However, arguably the most prevalent pursuit amongst quantum technologists to date, has been the construction of a universal fault-tolerant quantum computer. Though the physical environment which would serve as its hardware has not been unanimously agreed on yet, there has still been extensive research on the criteria/requirements a hardware-agnostic prototype must fulfill to be considered a candidate for a realizable quantum computer [14, 15]. Further research has also extended into how one could compare, and ultimately test, functioning quantum computers' advantage against classical computation [16, 17, 18], with a number of proposed algorithms a quantum computer alone may exploit to garner an advantage [19, 20, 21].

Quantum computers are to be the most compact and yet most powerful computational devices possible. Reasonable questions have been raised about counteracting the inherent fragility of quantum systems while maintaining control over them to enable the construction of a functional quantum device. Blueprints for the scaling of these quantum computer candidates have existed for some time [22, 23, 24, 25], with considerable recent progress being made [26, 27]. By far, one of the most promising and natural applications for quantum computers, which we have a solid foundation to believe in, is the same application that Feynman envisaged more than 40 years ago: the simulation of quantum systems [28, 29].

We know this to be a clear and obvious advantage as exact classical means of simulating these systems hits a limit of infeasability well before 60 Qubits [30]. Certain quantum hardware has surpassed this classical threshold in the number of physical qubits with high fidelity gate operations [31] and therefore novel findings even within the current 'noisy intermediate-scale quantum' (NISQ) devices are probable [32]. These developments are milestones in nature, but the task of scaling up these devices beyond the NISQ domain, to further increase the computational capacity, presents new difficulties in error-rate propagation and noise elevation [33, 34]. In fact, until the advent of Quantum Error Correction (QEC), the prospect of a universal, fault-tolerant quantum computer appeared far-fetched [35, 36]. The difficulty in useful QEC approaches however, is the requirement of even more physical qubits to protect the encoded information from the environment. This presents an argument that there may be limitation on how large (qubit-wise) a single quantum processor can be.

A proposal to circumvent this issue has been brought forward. Instead of sizing up a single-module quantum computer, that the computer itself be constructed as an array or ensemble of processors/modules, which are connected by 'quantum wires' [37, 38, 39]. These wires, formed by spin chains/permanently coupled qubits, may act as data transmission channels, or even take part in the computation themselves, in the form of entanglement generation to assist the modular ensemble with the processing of information [40, 41, 42]. To this end, there has been extensive research of the pre-engineering of these one-dimensional wires to achieve unit-fidelity state transfer, of initially encoded quantum information, from the beginning to the end of the chain. One of the most successful theoretical schemes, for which there has been experimental demonstrations of its efficacy [43], requires a strongly inhomogenous coupling profile [44, 45]. This prescription has not been implemented throughout different hardware, due to the inherent difficulty in tuning the inter-qubit interactions across the candidate substrates ubiquitously. It has therefore been suggested that a homogenous (or near-homogenous) coupling profile would be more desirable [40, 46].

In this thesis, we present an alternative model, with homogeneous coupling, using an optimization approach via a genetic algorithm. This model requires only the modulation of on-site energies to achieve high-fidelity state transfer or quasi-perfect state transfer (QPST). We will also discuss how these QPST schemes can be converted to perfect state transfer (PST) models, examining the trade-offs involved through further analysis using an inverse eigenvalue approach. Additionally, we explore the potential for experimental realizations of our proposal, including the degree of precision required. Through this investigation, we emphasize the importance of grounding theoretical modeling in experimental feasibility, ultimately with the aim of progressing the development of future quantum technologies. Previous research has discussed solutions of single, specific chain length and a corresponding tuning of a general harmonic potential [47, 48], or the creation of dual-site 'barrier' potentials for high transmission probability [49]. In contrast, the results presented here are systematic and offer a number of prescriptions for varied (odd and even) chain lengths with distinct 'families' of adjustments that may be made based on the spectral properties of the system, whilst still respecting the homogeneity of the inter-qubit coupling scheme.

1.1 Foundations of Quantum Computing

1.1.1 The Qubit

The primary contrast between means of quantum vs. classical computation, is the necessary distinction by how we define an irreducible 'bit' of information. In classical computation, a bit is typically represented by the state of a physical system, such as a transistor, which is relatively large compared to quantum scales. The bit can exist in one of two distinct states, corresponding to

$$(0) \quad or \quad (1),$$

which may be interpreted as functionality-dependent signals, such as

$$(\mathit{Yes/On}) \quad or \quad (\mathit{No/Off}).$$

The term 'bit', being a contraction of the term *binary digit*, popularized by Shannon in his famous 1948 paper [50] (though he attributes the first use of the word to John W. Tukey), has become foundational within the lexicon of theoretical computer science and information theory. Within quantum computing, there is a mathematical object that is analogous to the classical bit, the quantum bit or 'qubit' [51]. Instead of 0's and 1's, there are ket vectors $|0\rangle$ and $|1\rangle$, whose respective vector representations are conventionally

$$|0\rangle = \begin{pmatrix} 1 \\ 0 \end{pmatrix}, \quad |1\rangle = \begin{pmatrix} 0 \\ 1 \end{pmatrix}, \tag{1.1}$$

and serve as our quantum computational basis. From the standpoint of quantum mechanics, it is understood that unless a state has been 'acted upon' in some way, the most accurate description of its current nature is within a linear algebraic combination or 'superposition' of possible states

$$|\psi_A\rangle = \alpha|0\rangle + \beta|1\rangle, \tag{1.2}$$

where α and β are corresponding amplitudes to the probabilistic outcomes we've superimposed onto our basis of $|0\rangle$ and $|1\rangle$

$$\alpha = \langle 0|\psi_A\rangle, \qquad \beta = \langle 1|\psi_A\rangle,$$

resulting from the inner product between orthonormal basis states being $\langle i|j\rangle = \delta_{ij}$. This protean construction of $|\psi_A\rangle$ is expressed within a 2-dimensional complex vector space, known formally as a Hilbert space, denoted as $\mathcal{H}$. The principle of superposition exhibited by qubits introduces a form of functional-agnosticism, which can be leveraged in numerous ways due to the flexibility it offers in its mapping to a plethora of physical phenomena. So long as a quantum system, or a specific feature of it, can exist in (or rightly *between*) two distinct, well-defined levels—one state, its sister state, and a superposition of both—it may serve as a valid qubit, subject to further quality assessment. In fact, Feynman demonstrated this versatility of physical systems which may be considered as a qubit, in showcasing the MASER mode of the ammonia (NH_3) molecule, and its electric dipole moment either being anti-aligned $\mu_\downarrow$ ($|0\rangle$) or aligned $\mu_\uparrow$ ($|1\rangle$) with respect to a longitudinal electric field [52].

Origins of the probabilistic interpretation of α and β, within Eq.(1.2), stems from the projection of their statistical 'weight' formalized by the normalization condition [53]

$$|\alpha|^2 + |\beta|^2 = 1, \tag{1.3}$$

resultant from the insistence that the state vector, $|\psi_A\rangle$, is a unit vector

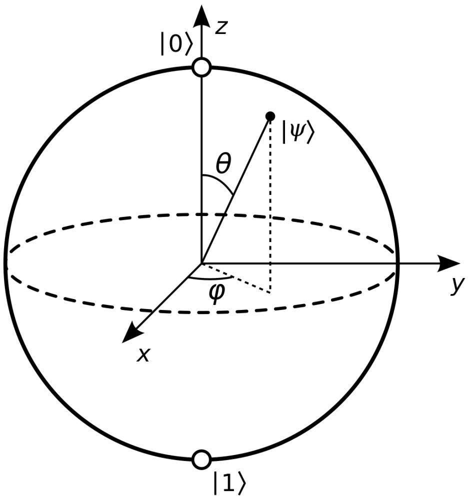

Figure 1.1: Bloch sphere representation of a state vector, $|\Psi\rangle$,

($\langle\psi_A|\psi_A\rangle = 1$) within the associated Hilbert space.

In defining $\alpha = \cos(\frac{\theta}{2})$ and $\beta = e^{i\varphi}\sin(\frac{\theta}{2})$ (thus fulfilling Eq.(1.3)) single qubits may be mapped to a vector extending out (from the origin) along the interior surface of what's known as the Bloch Sphere (See Fig.1.1) [54]. θ and φ within Fig.1.1, are numbers which define the polar and azimuthal co-ordinates, placing the end of the Bloch vector $|\psi\rangle$ throughout infinitely many points on the sphere, with its coordinates being indicative of the likelihood of measuring the outcome associated with an adjacent pole. It should be noted that these angles are angles between state vectors within the Bloch sphere representation, not within the Hilbert space itself. As spin-$\frac{1}{2}$ states, $|\uparrow\rangle$ and $|\downarrow\rangle$, of fermions are isomorphic to qubits [37, 55], Eq.(1.2) may be re-expressed as

$$|\psi_A\rangle = \alpha|\downarrow\rangle + \beta|\uparrow\rangle,$$

and thereby we may exploit the spin-$\frac{1}{2}$ degrees of freedom of fermionic quantum systems to map to the computational basis and vice versa.

1.1.2 Multiple Qubits

Moving out of the Bloch sphere representation and on to consider more than 2 degrees of freedom in the combination of the $|0\rangle$ and $|1\rangle$ states of a single qubit, we may observe 2 corresponding separable qubits $|\psi_A\rangle = \alpha|0\rangle + \beta|1\rangle$ and $|\psi_B\rangle = \gamma|0\rangle + \eta|1\rangle$ and defining $|\psi_C\rangle$ as a product of them

$$|\psi_C\rangle = |\psi_A\rangle \otimes |\psi_B\rangle = \alpha\gamma|00\rangle + \beta\gamma|10\rangle + \alpha\eta|01\rangle + \beta\eta|11\rangle, \tag{1.4}$$

where the tensor product $\otimes$ presents outcomes from $|\psi_A\rangle$ and $|\psi_B\rangle$ together. It should be noted that this is not the only form that two-qubit states can take. Any state vector that cannot be expressed in the form of Eq.(1.4), is described as an 'entangled state,' which provides a more general representation for multiple qubits. For convenience, we focus only on the product state form here. It can be appreciated readily that through the construction of $|\psi_C\rangle$, there has been an expansion in the total number of possible outcomes/basis states, in that the single qubit system (Eq.(1.2)) requires 2 distinct outcomes, and now, with the 2-qubit system (Eq.(1.4)), there are 4.

This demonstrates the dimensionality of, or the number of orthogonal states allowed within, the associated Hilbert space grows like 2^N, where N is the number of 2-level systems acting as qubits we have within our total system. This is exemplified clearly by the expression that any one state vector

$$|\psi\rangle = \sum_{n=1}^{2^N} a_n|\phi_n\rangle,$$

can be written as an expansion of its basis states $|\phi_n\rangle$ with unique coefficients a_n. Thus, the entire 2^N-set of $|\phi_n\rangle$ states are linearly independent vectors within the 2^N-vector space, and therein form a complete *basis* [56]. Quantum registers, unlike their classical counterparts, not only represent one of the 2^N possible states from the N-bit system, but all of the 2^N possible states simultaneously as a superposition of amplitudes. This allows for the exploitation of ‘quantum parallelism’, enabling quantum computers to process larger (compared to classical means of computation) pools of information concurrently [54]. We will discuss in greater detail in subsequent chapters, that the vector space we are interested in, concerning our current research, is a subspace (only examining single spin-flip/excitation subspaces) of a larger Hilbert space in which the total number of basis states grows like N, instead of 2^N.

1.1.3 Quantum Gates

In order for a quantum computer to process, store, transmit, and readout information in a similar way to its classical counterpart, in the highly advanced digital supercomputer, it needs to be able to work with quantum analogues of classical gate operations. These gate operations need to be able to manipulate qubits using quantum logic gates, by which the effect is a familiar computational process. In reviewing the classical single bit $\boldsymbol{NOT}$ gate, whose operation is defined by taking the (0) and (1) bits

$$\boldsymbol{NOT}(0) \rightarrow (1),$$

$$\boldsymbol{NOT}(1) \rightarrow (0),$$

and simply swapping them. The way to map this action to the qubit is non-trivial due to our quantum bit being in a combination of the outputs associated with $|0\rangle$ and/or $|1\rangle$. Swapping the outputs along with their corresponding amplitudes (Eq.(1.2)) does not alter the system’s overall behavior because quantum states are described by linear combinations, so we can instead consider swapping the amplitudes themselves as a $\boldsymbol{Q\text{-}NOT}$ gate

$$\boldsymbol{Q\text{-}NOT}|\psi_A\rangle = \alpha|1\rangle + \beta|0\rangle. \tag{1.5}$$

Using $\langle i|j\rangle = \delta_{ij}$ and Eq.(1.5), we can deduce the Bra-Ket [54] representation of $\boldsymbol{Q\text{-}NOT}$ to be

$$\boldsymbol{Q\text{-}NOT} = |0\rangle\langle 1| + |1\rangle\langle 0|.$$

Furthermore, noticing the matrix form of our computational basis (Eq.(1.1)) we find

$$\boldsymbol{Q\text{-}NOT} = \begin{pmatrix} 0 & 1 \\ 1 & 0 \end{pmatrix}, \tag{1.6}$$

which turns out to be conveniently the Pauli-X matrix, σ_x. It can be shown through similar treatment that all of the Pauli matrices are in fact quantum gates

$$\sigma^x = \begin{pmatrix} 0 & 1 \\ 1 & 0 \end{pmatrix}, \quad \sigma^y = \begin{pmatrix} 0 & -i \\ i & 0 \end{pmatrix}, \quad \sigma^z = \begin{pmatrix} 1 & 0 \\ 0 & -1 \end{pmatrix}. \tag{1.7}$$

and remarkably any such matrix/operator which fulfills the unitarity constraint $AA^\dagger = \hat{\mathbb{I}}$ also serves as a valid quantum gate. Some of the most prevalent quantum gate operations, along with their circuit symbols and output states, are shown in Table 1.1.

For single qubit gates, we can visualize their action as the state vector rotating within the Bloch sphere (Fig.1.1). For multiple qubits however, we require more intricate circuit designs, such as those exhibited within Table.1.2. The ability to map physical processes to the actions of logical gates, along with the knowledge of how one can decompose complicated functions into elements of a universal set of operations, serves as the foundation by which quantum computing may be built upon.

Gate	Circuit Symbol	$\|0\rangle$ Output	$\|1\rangle$ Output
$\mathbb{I}$ (Identity)	——	$\|0\rangle$	$\|1\rangle$
σ^x (Pauli-X)	$-\boxed{X}-$	$\|1\rangle$	$\|0\rangle$
σ^y (Pauli-Y)	$-\boxed{Y}-$	$i\|1\rangle$	$-i\|0\rangle$
σ^z (Pauli-Z)	$-\boxed{Z}-$	$\|0\rangle$	$-\|1\rangle$
H (Hadamard)	$-\boxed{H}-$	$\frac{1}{\sqrt{2}}(\|0\rangle + \|1\rangle)$	$\frac{1}{\sqrt{2}}(\|0\rangle - \|1\rangle)$

Table 1.1: Truth table and corresponding circuit symbols for single-qubit quantum gates.

Gate	Circuit Diagram	Matrix Representation
SWAP	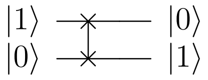	$\begin{pmatrix} 1 & 0 & 0 & 0 \\ 0 & 0 & 1 & 0 \\ 0 & 1 & 0 & 0 \\ 0 & 0 & 0 & 1 \end{pmatrix}$
CNOT	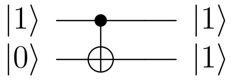	$\begin{pmatrix} 1 & 0 & 0 & 0 \\ 0 & 1 & 0 & 0 \\ 0 & 0 & 0 & 1 \\ 0 & 0 & 1 & 0 \end{pmatrix}$

Table 1.2: Multi-qubit quantum circuits, demonstrating the action of **SWAP** and **CNOT** gates along with their matrix representations in the computational basis.

1.1.4 Decoherence

The formal study of decoherence is an incredibly rich subject [57, 58, 59, 60] which has given valuable insight into ideas surrounding the correspondence principle, the measurement problem and the very idea of how physical systems become entangled with their environment. The coherences within our quantum mechanical description may be mathematically represented through the density operator of our previously introduced *pure state*, $|\psi_A\rangle$,

$$\hat{\rho}_A = |\psi_A\rangle\langle\psi_A|.$$

The matrix representation of $\hat{\rho}_A$ being (through taking the outer-product of Eq.(1.2))

$$\rho_A = \begin{pmatrix} |\alpha|^2 & \alpha^*\beta \\ \beta^*\alpha & |\beta|^2 \end{pmatrix}. \tag{1.8}$$

The off-diagonal terms in $\alpha^*\beta$ and $\beta^*\alpha$ serve as the coherence amplitudes, which are responsible for the 'quantumness' (interferences within double-slit experiments, for example) of our system, within a chosen basis. For a pure state, it is known that

$$\rho_A^2 = \rho_A.$$

However, for *mixed states* (defined by $\mathrm{tr}(\rho^2) < 1$), the system is no longer pure and the square of the density matrix will not be equal to itself, $\rho^2 \neq \rho$. Decoherence can be witnessed in the decay of the off-diagonal terms of Eq.(1.8); however, this effect is basis-dependent (unlike the purity of the state), as the presence of only diagonal entries within the density matrix does not necessarily indicate that the system behaves classically. Efforts are made to maintain and subsequently capitalize upon the presence of the coherence amplitudes, for means of computation. These amplitudes are essential for quantum computers to function, and thereby allowing sequential gate operations to occur reasonably. The time for a particular quantum system to lose its coherence terms and thereby *decohere*, is dependent upon factors such as the system size (effective scattering area), temperature and the coupling to its environment [59, 61].

1.2 Di Vincenzo's Criteria

In 2000, David Di Vincenzo outlined cogently the desiderata for physical implementations of a practically realizable quantum computer [15]. The criteria are as follows.

1.2.1 Scalability and Qubit Characterization

It is vital to characterize well the nature of the two-level ‘qubit’ from the candidate physical substrate. In the language of physics, we must have a comprehensive understanding of all of the effective interactions both within our system and necessary external connections. This provides a foundation as to how computation may be executed given external probing or the reliance on internal mechanisms. Relying on two quantized energy levels (serving as our computational basis) within atomic or ionic qubits, for instance, requires an ability to effectively decouple these energy levels from all the other possible energy levels within the system. This isolating procedure would be crucial in order for the system to be considered a useful and characterisable qubit.

To increase the overall quality of our qubit, efforts towards noise mitigation, isolation from the environment (as well as the rest of the system's Hilbert space for dimensions greater than 2), and decrease in gate operation errors are reasonable short-term goals [32]. As we are currently still residents of the NISQ era of quantum computers, further development within quantum error correction [34], along with experimental findings/refinement holds the greatest amount of promise in the increase in the total number of controllable qubits. For quantum computers to be able to solve certain tasks in which classical computation struggles earnestly to keep up, the number of physical Qubits required for the error corrected logical Qubits are of the order of millions [62, 63]. Given our leading hardware design still fits comfortably within the NISQ domain of $\sim 10 - 10^2$ qubits [31, 32], there are plenty of battles left to be won.

1.2.2 Initializing to a simple fiducial state, $|00000..\rangle$

This requirement may be summarized as the ability to prepare a known initial state (with confidence) repeatedly. The processing of information and interpretation of the output (both classically and in the quantum realm) becomes an increasingly incomprehensible task when the input is not well-known. Cooling techniques are often implemented within particular hardware such that the ground state is our referential fiducial state. Incorporating cooling techniques, however, takes time and can be complicated, especially when requiring to chill the system down to the μK-nK range [64]. An alternative preparation method, if possible, is to measure every qubit in the system and apply σ^x operations (Eq.(1.7)), if any $|1\rangle$ states are measured. This approach also manufactures the all-zero state, and can be useful, so long as the time required for the bit-flip operations is significantly less than the system's characteristic decoherence time (discussed more within the next subsection).

Onto this fiducial state, we may create and transmit excitations and have a clearer mapping between experimental procedure and the theoretical application of quantum gates. This particular criterion outlines the importance of setting conditions for reproduciblity of experiments. If we could model a perfect input, it would be a pure state with zero entropy. This picture however is shrouded in idealism (especially with larger and larger number of qubits). Nature has decided for us that we will have to make necessary compromises.

1.2.3 Decoherence time $\gg$ operation time

It is intuitive that we need our computational substrate to subsist long enough for the process of computation to occur. If we only had access to a classical computer for 5 minutes (as a metaphorical example, say someone else needed to use it urgently) but we had good reason to believe the amount of time we required to use it for our calculations was $\approx$ 10 minutes, then in this particular moment in time this computer isn't particularly useful to us. At least until the conditions improve. This logic is profoundly relevant when dealing with quantum computers due to the execution of complex quantum algorithms requiring a large number of gate operations and if these gate operations can only occur within a certain window of time (given current limitations in the laboratory or other hardware-specific concerns) we want to have confidence that our computation can take place.

The balancing act between perfect system isolation and the necessity of external interactions is central to this problem. Without very good isolation from the environment we lose the ability to exploit (or even observe) quantum effects, and without an ability to 'tell' the system what we want it to compute, there is no computation. The window of time we may refer to regarding specific hardware's decoherence eventuality is codified by the T_2 parameter [31, 64], often referred to as the 'transverse relaxation' or coherence time within the relevant literature. For future reference we will also define the time taken for a 2-Qubit gate to be τ_2.

1.2.4 Universal set of quantum gates

Within classical computation any function can be effectively built by a sequence of ***AND*** and ***NOT*** gates. This presents an argument of the set of ***AND*** and ***NOT*** procedures (or indeed physical processes which mimic them) are 'universal' within computation, as the execution of more complicated/intricate computation may be decomposed into a sequence of the elements within this set. It may be shown that any unitary transformation may in fact be decomposed into single qubit and ***CNOT*** gate operations [65]. The universal set itself is not a unique construction. Seth Lloyd, in fact, showed in 1995 that almost any quantum logic gate is computationally universal [66].

This universality grants us the ability for task computation, once it is known what physical processes mimic these gate operations satisfactorily. Having appropriately selected systems that allow for the universality of quantum gate procedures is key to creating a hospitable environment for the implementation of quantum algorithms.

1.2.5 Readout of qubit-specific outcomes

If we were able to perfectly isolate a quantum system there will come a time in which, if we expect to gain information, we will have to interact with it by reading an output. Through this interaction we effectively measure the system within an orthonormal measurement basis, and intuitively project the system to one of its eigenstates, as any singular moment will give us a singular result. We say a normalized state in $|\psi_A\rangle$, when measured, is acted upon by a measurement operator $\hat{W}_w$, with outcome w. Clearly, for the single qubit, $\hat{W}_w$ can only collapse $|\psi_A\rangle$ to $|0\rangle$ with $\hat{W}_0 = |0\rangle\langle 0|$ or $|1\rangle$ with $\hat{W}_1 = |1\rangle\langle 1|$. The post-measurement state, $|\psi_A'\rangle$, may therefore be shown to be

$$|\psi_A'\rangle = \frac{\hat{W}_w|\psi_a\rangle}{\sqrt{\langle\psi|\hat{W}_w{}^{\dagger}\hat{W}_w|\psi\rangle}},$$

where $\sum_w \langle\psi|\hat{W}_w{}^{\dagger}\hat{W}_w|\psi\rangle = 1$, satisfies the completeness relation [54]. Obtaining $|\psi_A'\rangle$ for specific hardware requires consideration for the nature of the qubit itself.

For ion trap quantum computers for instance, the laser-induced excitations from the ground state may serve as our two-level system [67], whilst for semiconductor quantum dots it is the energy signature obtained from fluorescence measurements, between the singlet and triplet state [68]. NMR even offers unique capabilities for 'weak' measurements through sampling the transverse magnetization throughout the entirety of the system, and therefore reducing the amount of disturbance on any one particular qubit [69]. Luckily, there are myriad ways in which one can gain information about a quantum system, and therein lies optimism for the pursuit of future decoherence minimizing readout procedures.

2

Spin Chains for Quantum Communication

2.1 Genesis as 'Quantum Buses'

In 2003 Sougato Bose pioneered the notion of exploiting the properties of systems which may be realistically described as linear chains of coupled spins, for purposes of quantum communication and information transfer [37]. He demonstrated that after waiting a period of time one can see that even an unmodulated chain governed by an isotropic Heisenberg exchange interaction may transfer an injected excitation or encoding across physical distances. He showed this through evolving a Heisenberg ferromagnet within an appropriately chosen magnetic field, from its ground state (all spins aligned with the z-axis) with one single excitation (one spin anti-aligned) encoded at the beginning of the chain, to eventually present high fidelity transfer to the opposite side.

Others, in reaction to this revelation, began the pursuit of constructing 'passive quantum network' designs [39] by deriving optimal pre-engineered protocols for these kinds of chains to yield perfect state transfer (PST) [39, 40, 44, 45, 46, 70, 71]. It's been well-established that for $N \geq 4$, PST is not to be expected with a constant coupling and on-site energy profile [44, 72, 73]. Therefore, for chains of N $\geq$ 4, we require one of the two to be altered in some manner for our system to accommodate high fidelity transfer, let alone PST.

2.2 Spin Models

A leading, widely-applicable model studied in the relevant literature, focusing on nearest-neighbor interaction spin chains and quantum communications, is the so-called Heisenberg exchange interaction [74] within an appropriately chosen external magnetic field

$$\hat{H}_{\mathrm{Heis}} = -2\sum_{i}^{N-1} J_{i,i+1}\mathbf{S}_i \cdot \mathbf{S}_{i+1} + \sum_{i=1}^{N} \varepsilon_i \mathbf{S}_i^z, \tag{2.1}$$

where $\mathbf{S}_i$ and $\mathbf{S}_{i+1}$ are the spin operators at sites i and $i+1$, respectively, and $J_{i,i+1}$ describes the 'exchange couplings' or simply the 'couplings' between neighboring sites, with site-dependent magnetic field strengths or 'on-site energies', ε_i. Note, that in applying an external magnetic field, we thereby break the $SU(2)$ symmetry [75], and the spin alignment is preferential to align or anti-align with it. Eq.(2.1) may be expanded in the following way

$$\hat{H}_{\mathrm{Heis}} = -\sum_{i=1}^{N-1} 2J_{i,i+1}\left(\hat{S}_i^x\hat{S}_{i+1}^x + \hat{S}_i^y\hat{S}_{i+1}^y + \hat{S}_i^z\hat{S}_{i+1}^z\right) + \sum_{i=1}^{N} \varepsilon_i \mathbf{S}_i^z. \tag{2.2}$$

Within condensed matter physics, the Heisenberg model serves as the 'effective' Hamiltonian for the dipole interaction of magnetic ions within a crystalline lattice structure at low-energy scales [76, 77]. In considering only spin-$\frac{1}{2}$ systems, the $\hat{S}^x$, $\hat{S}^y$, and $\hat{S}^z$ operators within Eq.(2.2) take the form (with a scaling of $\frac{\hbar}{2}$) of the Pauli operators $\hat{\sigma}^x$, $\hat{\sigma}^y$, and $\hat{\sigma}^z$ (Eq.(1.7)) in which their actions with respect to qubit operations (on site i) are well-known

$$\hat{\sigma}_i^x = (|0\rangle\langle 1| + |1\rangle\langle 0|)_i \quad ; \quad \hat{\sigma}_i^y = i(|0\rangle\langle 1| - |1\rangle\langle 0|)_i \quad ; \quad \hat{\sigma}_i^z = (|0\rangle\langle 0| - |1\rangle\langle 1|)_i.$$

We may therefore rewrite Eq.(2.2) in the computational basis, whilst ignoring the $\hat{S}_i^z\hat{S}_{i+1}^z$ terms, so we obtain the so-called XY model (also referred to as the XX Hamiltonian within relevant literature)

$$\hat{H}_{XY} = \sum_{i=1}^{N-1} J_{i,i+1}(|1\rangle\langle 0|_i \otimes |0\rangle\langle 1|_{i+1} + |0\rangle\langle 1|_i \otimes |1\rangle\langle 0|_{i+1}) + \sum_{i=1}^{N} \varepsilon_i |1\rangle\langle 1|_i, \tag{2.3}$$

of which our investigations are exclusively focused. It may be shown via the total number of excitations, $\hat{S}_{total} = \sum_i \hat{\sigma}^z$, that

$$[\hat{H}_{XY}, \hat{S}_{total}] = 0, \tag{2.4}$$

and therefore the total number of excitations from initialization to measurement is conserved. Eq.(2.4) also demonstrates that in commuting with the total spin operator, computational basis states are eigenstates of Eq.(2.2) only in cases where the Hamiltonian is completely diagonal (e.g., for states like $|0000..\rangle$ or $|1111..\rangle$) and therefore the dynamical evolution of the system can only be provoked through some sort of external intervention (discussed more in Sec.2.3.1)[39, 69]. Our Hamiltonian in Eq.(2.3), may be reformulated via its spin-operator representation, in terms of fermionic creation and annihilation operators ($\hat{c}^\dagger$ and $\hat{c}$) via the Jordan-Wigner transformation [78, 79]

$$\hat{H}_{XY} = \sum_{i=1}^{N-1} J_{i,i+1} \left(\hat{c}_i^\dagger \hat{c}_{i+1} + \hat{c}_{i+1}^\dagger \hat{c}_i \right) + \sum_{i=1}^{N} \varepsilon_i \hat{c}_i^\dagger \hat{c}_i, \tag{2.5}$$

where the hopping terms and on-site energies may be re-conceptualized exactly as a tunneling amplitude and chemical potential of the fermions respectively. Eq.(2.5) may be subsequently diagonalized to yield

$$\hat{H}_{XY} = \sum_{k=1}^{N} \lambda_k \hat{c}_k^\dagger \hat{c}_k, \tag{2.6}$$

where Eq.(2.6) is the Hamiltonian of a single non-interacting fermion which exists in the k_{th} energy eigenstate $|k\rangle$. As this Hamiltonian also describes non-interacting fermions, the computational basis state $|0\rangle$ corresponds to a vacuum state where no particle has been detected, whilst $|1\rangle$ corresponds to the presence of a maximum of a single particle. This equivalence between Eq.(2.5) and Eq.(2.3) demonstrates an ability to map the spin-$\frac{1}{2}$ XY model to a Hubbard model for non-interacting fermions [39]. The eigenvalues of both Eq.(2.3) and Eq.(2.5) (λ_n & λ_k), are constrained to a dispersion relation reminiscent of the tight-binding model [80]

$$\lambda_k = \varepsilon_k - 2J\cos\left(\frac{k\pi}{N+1}\right), \tag{2.7}$$

assuming $J_{i,i+1} = J$ for all i, with $k \in [1, 2, ..., N]$, which informs our intuition as to an allowance of the eigenvalues. The XY model Eq.(2.3) takes the form of a tridiagonal matrix

$$H_{XY} = \begin{pmatrix} \varepsilon_1 & J_{1,2} & \cdots & 0 & 0 \\ J_{1,2} & \varepsilon_2 & \cdots & 0 & 0 \\ \vdots & \vdots & \ddots & \vdots & \vdots \\ 0 & 0 & \cdots & \varepsilon_{N-1} & J_{N-1,N} \\ 0 & 0 & \cdots & J_{N-1,N} & \varepsilon_N \end{pmatrix}_{N\times N}, \tag{2.8}$$

within the site basis and through appropriate calculation of the matrix elements $\langle i|H_{ij}|j\rangle$. Alongside describing the interactions within naturally occurring systems and giving insight within the study of ferro/anti-ferromagnetism of materials, this Hamiltonian has also been used to successfully model a number of artificial qubit-hardware landscapes [69, 81, 82, 83, 84, 85, 86, 87].

2.3 Initialization

2.3.1 Zero State

The preparation of the all-zero state may come about in different ways, namely two for reference. Within an appropriately chosen magnetic field the orientation of the spins, at zero temperature, are aligned with each neighboring site with respect to the direction of the magnetic field axis

$$|000000000000000\rangle_{T=0}.$$

Therefore we may induce the zero, fiducial state through thermal cooling of the system to its ground state. However, in the case of a non-uniform/existent magnetic field we may measure each spin within the array. If all are measured to be down, $|0\rangle_i$ for all i, then we have successfully prepared the fiducial state. In the event we measure one site to be spin up, $|1\rangle_i$ at site i, we simply apply a spin flip operation, $\hat{\sigma}_i^x$, to that site (See Sec.1.2.2).

2.3.2 Initial State

The initialized system $|\psi_1\rangle$, in which our investigation is exclusively focused, is the single excitation deviation of the otherwise completely ferromagnetic linear spin chain

$$\hat{\sigma}_1^+|0000000\rangle = |1000000\rangle = |\psi_1\rangle, \tag{2.9}$$

represented here as a $N = 7$-site chain, where $\hat{\sigma_i}^{\pm} = (\sigma_i^x \pm i\sigma_i^y)$ either removes (-) or adds (+) a spin flip at site i. This translates to the ground state of a zero-temperature ferromagnet, with an initial spin flip or excitation exactly localized at the very beginning of the chain (site 1). It can be shown this single spin flipped chain is no longer an eigenstate of the XY model and therefore will evolve when acted on by the time evolution operator.

2.4 Natural Dynamics

The aim for linear register communication protocols is for an initial encoding to traverse to the opposite side of the chain at some predictable time t_m,

$$|\psi_1\rangle = |100...00\rangle \overset{t_m}{\to} |\psi_N\rangle = |000...01\rangle. \tag{2.10}$$

We may also illustrate this process concretely as a sequential spin-flip qubit operation

$$|\psi_1\rangle = |100...00\rangle \overset{t_m}{\to} \sigma_N^+\sigma_1^-|\psi_1\rangle = |000...01\rangle, \tag{2.11}$$

and in doing so highlighting the mapping between t_m and T_Q (See Sec.1.2.3). To be able to demonstrate the evolution of this system we evoke the Schrödinger equation for the appropriate time evolution operator corresponding to our time-independent Hamiltonian (Eq.(2.3)), $\hat{U}(t,0) = e^{-iH_{XY}t/\hbar}$. The action of the time evolution operator on a general state, $|\psi_0\rangle = \sum_{i=1}^{N} a_i|\phi_i\rangle$ where $|\phi_i\rangle$ are the eigenstates, imparts a time-dependence

$$\hat{U}(t,0)|\psi_0\rangle = \sum_{i=1}^{N} e^{-iH_{XY}t/\hbar} a_i|\phi_i\rangle = \sum_{i=1}^{N} a_i(t)|\phi_i\rangle = |\psi_0(t)\rangle, \tag{2.12}$$

where the evolution of the state is orchestrated by H_{XY}. The success of the the pre-selected values of $J_{i,i+1}$ and ε_i, in terms of allowing high likelihood for state transfer between sites, is codified by the transfer fidelity over time

$$F(t) = |\langle\psi_N|e^{-iH_{XY}t/\hbar}|\psi_1\rangle|^2, \quad 0 \leq F(t) \leq 1. \tag{2.13}$$

Fidelity values which surpass $66.6\overline{6}\%$, presents an advantage over classical means of communication and may be considered 'useful' [38, 88]. Scores of 100% (up to a reasonable level of numerical precision), which are periodic/recurrent in time, signify perfect state transfer (PST).

3

Quantum State Transfer: Necessary-Sufficient Conditions and Known Protocols

3.1 Mirror Symmetry

Achieving PST within linear one-dimensional chains, comprising N-sites, necessitates that the system's Hamiltonian exhibit a 'mirror symmetry' with respect to the chain's mid-point [38, 44, 89]. This requires that the single excitation subspace matrix representation of our Hamiltonian (Eq.(2.3)) commutes with the corresponding mirror operator $\hat{M}$

$$M = \begin{pmatrix} 0 & 0 & \cdots & 0 & 1 \\ 0 & 0 & \cdots & 1 & 0 \\ \vdots & \vdots & \ddots & \vdots & \vdots \\ 0 & 1 & \cdots & 0 & 0 \\ 1 & 0 & \cdots & 0 & 0 \end{pmatrix}_{N\times N} , \tag{3.1}$$

which takes the form of this $N \times N$ matrix. Its operation on the $N \times 1$ initial state vector, $|\psi_1\rangle$, (Eq.(2.9)) is

$$\hat{M}|\psi_1\rangle = \hat{M}|100..00\rangle = |000..01\rangle = |\psi_N\rangle. \tag{3.2}$$

In this way $|\psi_N\rangle$ may be defined as the 'mirror image' of $|\psi_1\rangle$ with respect to mirror operation. Note, the commuting of our single-excitation Hamiltonian matrix with the mirror matrix of Eq.(3.1)

$$[\hat{H}_{XY}, \hat{M}] = 0, \tag{3.3}$$

therefore enforces a necessary condition for state mirroring (Eq.(3.2)) to be

$$\varepsilon_i = \varepsilon_{N-i+1}, \tag{3.4}$$

$$J_{i,i+1} = J_{N-i,N-i+1}, \tag{3.5}$$

for all $i \in (1, 2, 3, .., N-1)$. For any system described by $|\psi_1\rangle$, this state can be expressed as a linear combination of its symmetric $|\psi\rangle_+$, and anti-symmetric $|\psi\rangle_-$ components

$$|\psi_1\rangle = \frac{1}{\sqrt{2}}(|\psi\rangle_+ + |\psi\rangle_-), \tag{3.6}$$

their respective definitions as eigenstates of $\hat{M}$ being

$$|\psi\rangle_+ = \frac{1}{\sqrt{2}}(|\psi_1\rangle + \hat{M}|\psi_1\rangle) \quad \text{and} \quad |\psi\rangle_- = \frac{1}{\sqrt{2}}(|\psi_1\rangle - \hat{M}|\psi_1\rangle),$$

with eigenvalues of $+1$ (for symmetric/even states) and -1 (for anti-symmetric/odd states). Due to the commuting of $\hat{H}_{XY}$ and $\hat{M}$ (Eq.(3.3)), the eigenstates of $\hat{H}_{XY}$ must have definite symmetry/parity (either ± 1) under $\hat{M}$ operation. The symmetric and anti-symmetric components expanded over their even and odd parity eigenstates $|\phi_j\rangle_+$ and $|\phi_l\rangle_-$ are respectively

$$|\psi\rangle_+ = \sum_{j=1}^{n_{\text{even}}} a_{j,+}|\phi_j\rangle_+ \quad \text{and} \quad |\psi\rangle_- = \sum_{l=1}^{n_{\text{odd}}} a_{l,-}|\phi_l\rangle_-, \tag{3.7}$$

with coefficients $a_{j,+}$ and $a_{l,-}$ and the number of even states, n_{even}, and number of odd states, n_{odd}, correspondingly satisfying $n_{\text{even}} + n_{\text{odd}} = N$. The system's adherence to mirror symmetry is captured by the action of the mirror operator $\hat{M}$ on these eigenstates, yielding

$$\hat{M}|\psi\rangle_+ = +|\psi\rangle_+ = +\left(\sum_{j=1}^{n_{\text{even}}} a_{j,+}|\phi_j\rangle_+\right), \tag{3.8}$$

and

$$\hat{M}|\psi\rangle_- = -|\psi\rangle_- = -\left(\sum_{l=1}^{n_{\text{odd}}} a_{l,-}|\phi_j\rangle_-\right), \tag{3.9}$$

therefore,

$$\hat{M}|\psi_1\rangle = \frac{1}{\sqrt{2}}(|\psi\rangle_+ - |\psi\rangle_-) = |\psi_N\rangle. \tag{3.10}$$

This results in unit fidelity (Eq.(2.13)) between the mirrored twin state vector $\hat{M}|\psi_1\rangle$ and the time evolved state $|\psi_1(t)\rangle$, so long as the state at some time mirrors itself, as required for perfect state transfer. The mirroring process necessitates some passage of time, which instigates the identification of a characteristic time, t_m. Within our framework of a time-independent Hamiltonian, we can be assured that even and odd states (formally symmetric and anti-symmetric states), will remain even and odd throughout the duration of the eigenstates' evolution [53], via the time evolution operation discussed previously (Eq.(2.12)). Therefore if we want the transfer fidelity (Eq.(2.13)) at some time t_m (the mirroring time), to be *exactly* equal to 100%, we require that [71]

$$e^{-iH_{XY}t_m/\hbar} = e^{-i\alpha}\hat{M}, \tag{3.11}$$

for some global dynamical phase α. Requiring Eq.(3.11) constrains our Hamiltonian and thus its spectrum. When this condition holds, the time evolution of the system will generate Eqs.(3.8) and (3.9) on the component eigenstates, which are necessary for PST. We may show from Eq.(2.13) and Eq.(3.2) that

$$\begin{aligned} F(t_m) &= |\langle\psi_N|e^{-iH_{XY}t_m/\hbar}|\psi_1\rangle|^2 \\ &= |\langle\psi_N|e^{-i\alpha}\hat{M}|\psi_1\rangle|^2 \\ &= |\langle\psi_N|\psi_N\rangle|^2 = 1, \end{aligned} \tag{3.12}$$

signifying the accomplishment of PST across an arbitrary N-site chain, given a Hamiltonian and corresponding spectrum that fulfills a required condition.

3.2 Spectral Considerations

Alongside the mirror symmetry, the eigenvalues of our Hamiltonian (Eq.(2.8)) play an important role in the capacity for the chain to transmit information effectively. Recalling that for the condition of Eq.(3.11) to hold, there must be constraints on the spectrum of our system. We will illustrate the nature of these constraints with an example for $N = 4$.

Consider a $N = 4$-site spin chain with an equally spaced energy spectrum given by

$$\lambda_n \in \{3\alpha, \alpha, -\alpha, -3\alpha\}, \tag{3.13}$$

where the spacing between sequential eigenvalues $\Delta\lambda_{n,n+1} = 2\alpha$. The eigenstates exhibit an alternating symmetry, from the highest eigenenergy (even) to the lowest (even for odd-site chains, odd for even-site chains). When evolving the even and odd symmetry eigenstates (with $\hbar = 1$), one may determine the time at which the system mirrors itself. For the even symmetry eigenstates, the time evolution is

$$|\psi(t)\rangle_+ = a_{3\alpha}e^{-i3\alpha t}|\phi_{3\alpha}\rangle + a_{-\alpha}e^{i\alpha t}|\phi_{-\alpha}\rangle,$$

and for the odd symmetry eigenstates, it is given by

$$|\psi(t)\rangle_{-} = a_{\alpha}e^{-i\alpha t}|\phi_{\alpha}\rangle + a_{-3\alpha}e^{3i\alpha t}|\phi_{-3\alpha}\rangle.$$

Setting $t = \frac{\pi}{2\alpha}$, the eigenstates evolve as follows. For the even symmetry eigenstates

$$\begin{aligned}|\psi\left(\frac{\pi}{2\alpha}\right)\rangle_{+} &= a_{3\alpha}e^{-i\frac{3\pi}{2}}|\phi_{3\alpha}\rangle + a_{-\alpha}e^{i\frac{\pi}{2}}|\phi_{-\alpha}\rangle, \\ &= e^{i\frac{\pi}{2}}\left(a_{3\alpha}e^{-i2\pi}|\phi_{3\alpha}\rangle + a_{-\alpha}|\phi_{-\alpha}\rangle\right), \\ &= e^{i\frac{\pi}{2}}|\psi(0)\rangle_{+},\end{aligned}$$

and for the odd symmetry eigenstates

$$\begin{aligned}|\psi\left(\frac{\pi}{2\alpha}\right)\rangle_{-} &= a_{\alpha}e^{-i\alpha\frac{\pi}{2\alpha}}|\phi_{\alpha}\rangle + a_{-3\alpha}e^{3i\alpha\frac{\pi}{2\alpha}}|\phi_{-3\alpha}\rangle, \\ &= e^{i\frac{\pi}{2}}\left(a_{\alpha}e^{-i\pi}|\phi_{\alpha}\rangle + a_{-3\alpha}e^{i\pi}|\phi_{-3\alpha}\rangle\right), \\ &= -e^{i\frac{\pi}{2}}|\psi(0)\rangle_{-}.\end{aligned}$$

The even and odd eigenstates acquire the same global phase, $e^{i\frac{\pi}{2}}$, with a relative minus sign for the odd states. Thus, it can be analytically observed that PST is guaranteed at time $t = \frac{\pi}{2\alpha}$ (referring to Eq.(3.10)), for a configuration corresponding to an equidistant energy spectrum. It has also been demonstrated that, more generally, the ratio of the difference between sequential eigenvalues must be rational for PST [44, 72]. This may be shown clearly in the inherent periodicity of a PST-accommodating, mirror symmetric system, in that when at time $2t_m$

$$|\langle\psi_1|e^{-2iHt_m}|\psi_1\rangle| = |\langle\psi_1|\psi_1(2t_m)\rangle| = 1, \tag{3.14}$$

as $\hat{M}^2 = \hat{\mathbb{I}}$ and as expected after a state perfectly mirrors at time t_m, it will return to the initial state with unit fidelity at time $2t_m$. Writing the evolved initial state $|\psi_1(2t_m)\rangle$ in the energy eigenbasis $|\phi_n\rangle$

$$|\psi_1(2t_m)\rangle = \sum_{n=1}^{N} b_n e^{-2i\lambda_n t_m} |\phi_n\rangle,$$

and imposing

$$|\psi_1(2t_m)\rangle = e^{i2\theta} \sum_{n=1}^{N} b_n |\phi_n\rangle,$$

(with θ as a phase constant, independent of n) we may therefore present the condition

$$2\lambda_n t_m - 2\theta = 2k_n\pi,$$

where k_n is simply an integer. We may take the difference of sequential eigenvalues

$$2t_m(\lambda_n - \lambda_{n+1}) = 2\pi(k_n - k_{n+1}), \tag{3.15}$$

thereby removing the phase constant 2θ, and dividing by another sequential non-degenerate eigenvalue pair λ_o and λ_{o+1} to remove the t_m dependence we find that

$$\frac{\lambda_n - \lambda_{n+1}}{\lambda_o - \lambda_{o+1}} = \frac{k_n - k_{n+1}}{k_o - k_{o+1}} \in \mathbb{Q}, \tag{3.16}$$

with $\mathbb{Q}$ indicating for the set of all rational numbers. This condition demonstrates that the ratio of differences between any sequential eigenvalue pairs must be rational to ensure constructive phase alignment for PST. An equivalent condition to Eq.(3.16), which is useful for spin chain construction, is the difference between any sequential eigenvalue pairs being

$$\lambda_{n+1} - \lambda_n = \frac{\pi O_{n,n+1}}{t_m}, \tag{3.17}$$

where $O_{n,n+1}$ is simply a pair-dependent odd integer [70, 89]. PST necessitates $O_{n,n+1}$ (as well as the differences of $k_n - k_{n+1}$ from Eq.(3.15)) to be an odd integer to ensure the alternating symmetry between the eigenstates with even and odd parity (Eqs.(3.8) & (3.9)). Any spectra which is consistent with Eq.(3.17) thereby guarantees Eq.(3.11). Therefore, any XY Hamiltonian with eigenvalues that fulfil Eq.(3.17) will elicit PST through its dynamics. If the spectrum itself exhibits symmetry about its center, such as a linear spectrum, it may be written as

$$\lambda_n = -\lambda_{N-n+1}, \quad \text{for } n \in [1, 2, ..., N], \tag{3.18}$$

with the consequence that the diagonal elements of our mirror symmetric matrix are confined to be a site-independent constant $\varepsilon_i = \varepsilon$ for all i [89]. Therefore, if we desire our system to harbor some variation of the on-site energies, we require a non-symmetric spectrum.

3.3 PST Protocols

3.3.1 Inhomogeneous Coupling Configurations ($\varepsilon_i = \varepsilon$)

To begin, we consider models with uniform and constant on-site energies. A prominent coupling model known for PST, with experimental support for its transfer efficacy [43], is

$$J_{i,i+1} = J_0\sqrt{(N-i)i}, \tag{3.19}$$

where J_0 sets the scale for the hopping amplitudes [44, 45]. This model is demonstrably powerful in that it is a general solution for N-site chains. Also, due to the linearity of its spectra (equidistant eigenvalues), it sets a referential speed limit for quantum information transfer through spin chains [90], not to imply there cannot be others which may match its swiftness in information propagation. We can observe from Fig.3.1, using a $N = 31$-site chain as an example, the coupling trend across the chain, the associated transfer fidelity dynamics and the linearity of the spectrum for this protocol.

Unfortunately, the strong inhomogeneity required of the couplings, which worsens with increasing system size N, presents difficulty in experimental implementation. Namely the energy difference between the maximum coupling value, J_{max}, and the minimum couplings towards the outer-sites, leads to an elevated susceptibility to external noise at either ends of the chain, arising from the environment-dependent imprecision of the values. It is due to these concerns which led others to focus instead on a coupling scheme

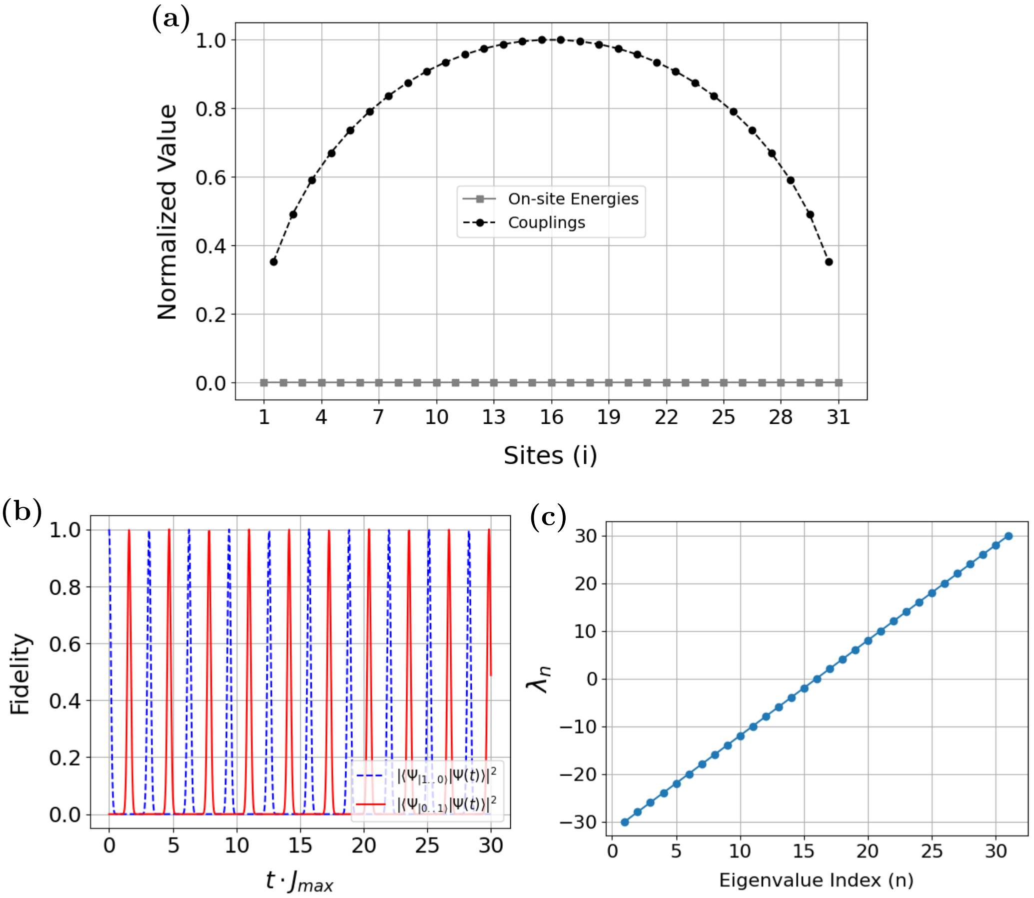

Figure 3.1: The coupling configuration (a) along the sites of the chain (Eq.(3.19)), associated dynamics (b) and spectrum (c), for a $N = 31$-site XY chain. The 'Normalized Value' along the y-axis of (a) is recorded as the dimensionless unit of relative values $(\frac{J_{i,i+1}}{J_{max}})$, whilst (c) λ_n are in units of J_{max}.

which only required minimal alterations to the couplings [46], as this would effectively quash the outer-site susceptibility issue and highlights an alternative scheme which still accomplishes PST. The proposed spectrum within [46] follows closely the dispersion relation of the spin model (Eq.(2.7)) though maintaining the spacing such that Eq.(3.17) and Eq.(3.18) are satisfied

$$\lambda_n \in \left\{ \begin{array}{cccccccc} 0, & \pm 21, & \pm 40, & \pm 61, & \pm 80, & \pm 97, & \pm 116, & \pm 131, \\ \pm 146, & \pm 161, & \pm 172, & \pm 183, & \pm 192, & \pm 199, & \pm 204, & \pm 207 \end{array} \right\}.$$

An example for the 31-site chain can be found within Fig.3.2 displaying the coupling trend across the chain, the transfer fidelity dynamics, and the dispersion-like spectrum. However, now due to the minimal variation required, the differences between coupling values require a level of precision which may be currently unrealistic. As an example of the level of precision required for the spectrum proposed for $N = 31$, it may be shown that it achieves 99.8%[1] transfer fidelity when truncating the exact coupling values to 4 significant figures (in which the rounding to numbers of significant figures follows conventional arithmetic rounding; 1235, [4 s.f.] $\rightarrow$ 1240, [3 s.f.]) but falls to $\approx$ 50% when valued up to 2 s.f. in the same time frame of $t \cdot J_{max} = 30$ (Table 3.1). For comparison, the coupling profile of Eq.(3.19) maintains transfer fidelity of 96.5% when rounded to 2 s.f., thereby demonstrating that what the scheme lacks in current experimental wide-scale applicability, it compensates for within the environments it may be produced in, with durability up to 2 s.f., where after it eventually falls down to $\sim$ 50% also.

---

[1] It can be shown that this protocol achieves transfer fidelities of 99.99..% with periodicity, which is demonstrative of PST, but is lower (99.8%) when discussed here, due to the level of precision required in the coupling values for PST exceeding 4 significant figures, which is the highest we present within this thesis.

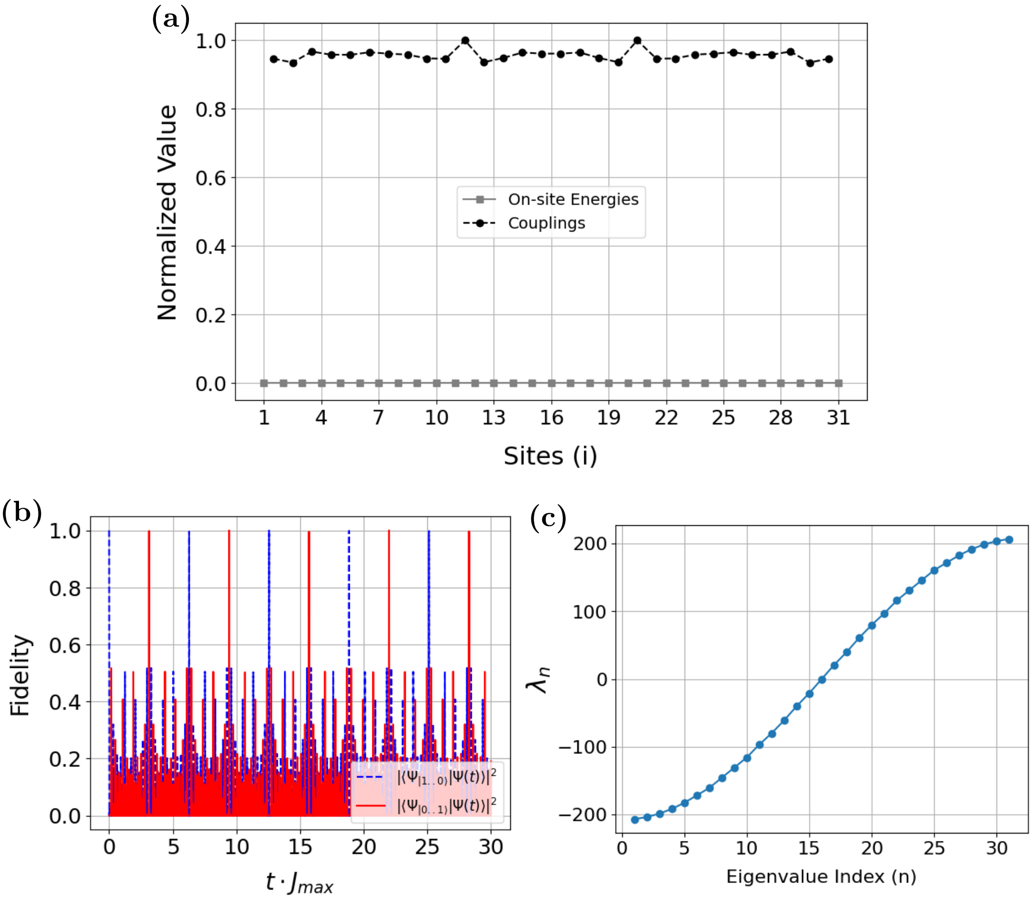

Figure 3.2: The coupling configuration proposed by Karbach-Stolze (a), with relative difference in the coupling throughout the chain being $\sim 3\%$. It can be seen from (b) that PST is still acquired within eigenvalues which are chosen such that they are closely representative of the dispersion relation (c). The 'Normalized Value' along the y-axis of (a) is recorded as the dimensionless unit of relative values ($\frac{J_{i,i+1}}{J_{max}}$), whilst (c) λ_n are in units of J_{max}.

Configuration	4 s.f.	3 s.f.	2 s.f.	1 s.f.
Christandl-Nikolopoulos [44, 45]	99.9%	99.9%	96.5%	44.9%
Karbach-Stolze [46]	99.8%	85.6%	52.9%	52.4 %

Table 3.1: Comparison of the degree of precision required for high-fidelity state transfer between two well-cited models.

3.3.2 Alternative Configurations ($\varepsilon_i \neq \varepsilon$)

Albanese et.al. [71] proposed another spectrum which is general in N, is quadratic instead of linear, and may be shown to violate Eq.(3.18) and therefore incurs a variation to the diagonal elements of the XY Hamiltonian. This variation in the on-site energies creates a negative parabola (similar to the structure of the relative coupling values exhibited within previous coupling scheme of Eq.(3.19)) along with the variation within the coupling, thus creating a model in which both form a negative parabolic structure to attain PST. The authors subsuquently chose appropriate Zeeman terms such that the diagonal elements all cancel out, resulting in a close resemblance to the original Christandl-Nikolopoulos scheme [44, 45].

Yung-Bose [40] also proposed a spectrum, for a 4-site chain, in which there is a discontinuous 'push' between the top-two eigenvalues, of an otherwise equidistant spectrum

$$\lambda_n \in \left\{ \;1, \quad 2, \quad 3, \quad 2(m+1)\; \right\} \quad \text{for } m \geq 1.$$

This spectrum also satisfies the necessary spectral conditions, and due to its discontinuity it necessitates site-dependence of the on-site contributions. This scheme, alongside Albanese et.al., evokes a negative parabolic structure of both the on-site energies and the couplings. The differences between the outer-site couplings and the couplings towards the center are still quite large ($\frac{J_{1,2}}{J_{max}} = 69.5\%$), and the on-site energies must now also be externally modulated for PST. Therefore, it is not immediately clear why one would choose to utilize this spectrum instead of the aforementioned all-coupling proposals. The matrix elements of Eq.(2.3), for this particular proposal though were not analytically but numerically derived from a general formula, which was itself obtained through an inverse eigenvalue method. We will discuss more of the background and execution of this approach within Sec.4.2.

3.3.3 p-Spectra

We now present a novel non-symmetric spectrum that is expected to produce PST. This has been devised by the York research group and preliminary results were presented in [91]. Here we present more detailed results, with a paper to follow [92]. We start with a $N = 4$ example, analogous to that of Eq.(3.13), and then present detailed analysis of the $N = 3$ case.

Consider, instead of a relative 'push' between the top two eigenvalues as previously described, the top two eigenvalues to be 'pinched' by the inverse of an odd integer p, such that the spacing between them is $\frac{1}{p}$ of the spacing throughout the rest of the spectrum. For instance, if we consider a $N = 4$-site chain with a mostly equidistant eigenvalue spacing of 2α, if the spacing between our top two eigenvalues were pinched by a strength of $p = 3$, our spectrum becomes

$$\lambda_n \in \{5\alpha/3, \alpha, -\alpha, -3\alpha\},$$

as the highest energy eigenvalue $\frac{5\alpha}{3}$ is equal to α (second highest eigenvalue)$+ \frac{2\alpha}{p}$. From Eq.(3.17) this spectrum translates to

$$O_{n,n+1} = \begin{cases} 3 & \text{for } n = 1, 2, \ldots, N-2 \\ 1 & \text{for } n = N-1, \end{cases}$$

and thereby satisfies the eigenvalue conditions for PST. To ascertain the time for state mirroring we observe again the time evolution of the symmetric and anti-symmetric components of our state vector

$$|\psi(t)\rangle_+ = a_{5/3\alpha} e^{-i5\alpha t/3} |\phi_{5/3\alpha}\rangle + a_{-\alpha} e^{i\alpha t} |\phi_{-\alpha}\rangle,$$

and

$$|\psi(t)\rangle_- = a_\alpha e^{-i\alpha t} |\phi_\alpha\rangle + a_{-3\alpha} e^{3i\alpha t} |\phi_{-3\alpha}\rangle.$$

It can be ascertained that unlike the example of a linear spectra Eq.(3.13), $t = \frac{\pi}{2\alpha}$ will not suffice for all of the eigenstates to mirror invert. If we instead set $t = \frac{3\pi}{2\alpha}$ and evolve our states we find

$$\begin{aligned} |\psi\left(\frac{3\pi}{2\alpha}\right)\rangle_{+} &= e^{i\frac{3\pi}{2}}\left(a_{5/3\alpha}|\phi_{5/3\alpha}\rangle + a_{-\alpha}|\phi_{-\alpha}\rangle\right), \\ &= e^{i\frac{3\pi}{2}}|\psi\left(0\right)\rangle_{+}, \end{aligned}$$

and

$$\begin{aligned} |\psi\left(\frac{3\pi}{2\alpha}\right)\rangle_{-} &= -e^{i\frac{3\pi}{2}}\left(a_{\alpha}|\phi_{\alpha}\rangle + a_{-3\alpha}|\phi_{-3\alpha}\rangle\right), \\ &= -e^{i\frac{3\pi}{2}}|\psi\left(0\right)\rangle_{-}, \end{aligned}$$

acquire a global phase with a relative (±) sign, thus establishing the mirroring time, $t_m = \frac{3\pi}{2\alpha}$. It may be shown through similar treatment, that the time for perfect state mirroring to occur from this upper-eigenvalue pinch spectrum is

$$t_m = \frac{p\pi}{2\alpha}. \tag{3.20}$$

We should therefore have to wait incrementally longer for each whole value increase of p, to the next odd integer ($1 \rightarrow 3 \rightarrow 5$ etc., due to the necessity of satisfying Eq.(3.17)). For a detailed analytical discussion we may begin with an $N = 3$, XY spin chain. For $N = 3$, exact PST results from equal couplings and with zero on-site energies, generating an equally-spaced spectrum, as the very simplest example of Eq.(3.19). However, we can introduce on-site energy dependence and explore pinching the spectrum by setting $\varepsilon_1 = \varepsilon_3 = \varepsilon$, $\varepsilon_2 = 0$ and all $J_{n,n+1} = 1$ for simplicity. Using Eq.(2.3) we may derive the following Hamiltonian matrix

$$H_{XY_{(N=3)}} = \begin{pmatrix} \varepsilon & 1 & 0 \\ 1 & 0 & 1 \\ 0 & 1 & \varepsilon \end{pmatrix}. \tag{3.21}$$

The eigenvalues of Eq.(3.21) are $\lambda_1 = \varepsilon$ and $\lambda_{2,3} = \frac{\varepsilon}{2} \pm \frac{\sqrt{\varepsilon^2+8}}{2}$, and through further algebra, taking the eigenvalue spacing between the highest eigenvalues to be $\frac{1}{p}$ of the lowest, an expression to relate the p-factor to the value of ε is found to be

$$\varepsilon = \sqrt{\frac{2}{p}} \cdot (p-1). \tag{3.22}$$

This demonstrates that this spectrum arises when the strengths of ε_i are minimal at the midpoint of the chain, and maximal at the ends. This provokes further tuning efforts to be directed towards optimizing on-site energy values, for larger N, guided by an auxiliary search for configurations whose spectra match the pre-selected p-values.

4

Numerical Methods: Spin Chain Construction

4.1 Genetic Algorithm

For the genetic algorithm (GA) work detailed in this thesis, I developed a new fitness function, as described in Eq.(4.1). In addition, I tailored the mutation process of the previously-existing code, referenced in [93], to suit the specific needs of this research.

4.1.1 Background and Fitness

Determining an on-site energy and/or coupling profile which maximizes the transfer fidelity across an N-site chain can be effectively addressed through evolutionary computation, specifically utilizing a genetic algorithm [93, 94]. This algorithmic process generally commences with an initial population of potential solutions, which are then subjected to a Darwinian selection process based on their performances, as assessed by a predefined fitness function [95, 96]. The fitness function effectively guides the genetic algorithm towards a solution which outperforms others with regard to a specific set of traits. A mutation process—either fixed or dynamically varying—then either expands or narrows the exploration within the search space, balancing the trade-off between global exploration and convergence to local optima. To search for high-fidelity configurations forming from a desired spectrum (tuned by a selected p-value, see Sec.3.3.3), the fitness function was modified from the original code as follows

$$f(F_{max}, \upsilon; Q, p, \sigma_E) = \aleph((A \cdot F_{max}) - (B \cdot \upsilon)), \tag{4.1}$$

where F_{max} is the maximum fidelity score achieved by the configuration within the time frame of evaluation, υ is the cumulative penalty associated with the desired spectrum

$$\upsilon = \left| Q - \frac{1}{p} \right| + \sigma_{E_n}, \tag{4.2}$$

formed by a Q-factor

$$Q = \frac{\Delta E_{N-1,N}}{\left(\prod_{n=1}^{N-2} \Delta E_{n,n+1} \right)^{\frac{1}{N-2}}},$$

as well as the standard deviation

$$\sigma_{E_n} = \sqrt{\frac{1}{N-2} \sum_{n=1}^{N-2} (\Delta E_{n,n+1} - \langle \Delta \bar{E} \rangle)^2},$$

of the eigenvalue spacings, apart from the reduced spacing between the highest two energy levels, $\Delta E_{N-1,N}$. The spectral penalty υ is minimized when $Q \approx \frac{1}{p}$, where we have a pre-defined value for p, therby optimizing the desired rational spacing, and when the variance of the eigenvalue spacings σ_{E_n} is relatively small. The fitness function was designed to optimize both high fidelity and specific spectral spacing as previous findings indicated that high-fidelity solutions with homogeneous coupling were achievable only for particular eigenvalue spectra [91]. The previous fitness function used within [91, 93], explored solutions which occurred with high-fidelity but also optimized for fastest time of transfer. Within Eq.(4.1), A and B are adjustable scaling factors, giving relative weights between the fidelity and spectral penalties, whilst $\aleph$ is the normalization

$$\aleph = (A \cdot F_{\max} + B \cdot \upsilon)^{-1}, \tag{4.3}$$

so that the fitness is scaled by the combination of the largest contributions of the penalties and the fitness values falls within the range $[0 - 1]$. It becomes clear that if A is chosen such that $A \gg B$, the genetic algorithm will find configurations which lead to purely higher-fidelity configurations with little consideration for the spacing between eigenvalues within the spectrum. The reverse is true when $A \ll B$, where the genetic algorithm will search for configurations which have the most desirable spectra and fidelity is a lesser consideration. Particularly for smaller chain lengths (such as $N = 3, 4$), A was selected to be of the order of B ($A \approx B$), to give approximately equal weight to the fidelity and spectra, whilst for higher order N-site chains, there was a larger weight placed on the fidelity ($A > B$).[1]

4.1.2 Algorithm Execution

The genetic algorithm begins with the selection of an individual created with a randomised on-site Hamiltonian configuration and equal couplings $J_{i,i+1} = 1$, from a population of the desired form (Eq.(2.8)). A subsequent mutation function takes the individual from the population and randomly alters the diagonal of the individual by values within a specified range (1-10 throughout all of the iterations discussed here). It had been decided that in the interest of preserving mirror symmetry about the centre of the chain (Eq.(3.4)), as well as greatly narrowing the search space and subsequently the computational taxation required, that the algorithm should only consider

---

[1] There is an expectation of a relative saturation of higher fidelity solutions within smaller N-site chains [38].

mirror symmetric individuals. This is enforced throughout the mutation process via the mutated offspring being mirrored about its centre, see Fig.4.1, and then subsequently passed onto the fitness evaluation within the genetic algorithm.

The natural dynamics of the system are then observed, recording the maximum fidelity attained within the allotted time window, the spacing of the energy spectrum, and the standard deviation of the spacing between the eigenvalues. The information about the individual is then indexed within the genetic algorithm, and its fitness score assessed via the specification defined by the fitness function Eq.(4.1). The crossover operation to proliferate information to the next generation of prospective solutions (offspring) then follows and is in-line with previous research where an evenly-distributed amount of genetic information, between selected parents, are exchanged to serve as the genetic material for their children [93].

This exchange between the previous generation occurs with equal probability so each parent has an opportunity to pass on 50% of their respective encoding. Iterations of these altered individuals, over sufficiently large generations, are selected with increasing fitness scores until the fittest 'Darwinian individual' is returned once the algorithm successfully terminates. The parameters for generations, initial population size, and mutation rate (including its evolution) were selected to mirror the methodology employed in prior research on adaptive quantum device design and are shown in Table.4.1 [93].

Generations	**Population – Size**	**Mutation – Rate**
200	1024	*20%

Table 4.1: The optimization parameters employed for all of the data presented within Sec.5. *Note, though the mutation rate is set to 20%, it was chosen to decrease, as a function of the number of generations, to increase the exploration of the local optima.

The primary alterations from the methodology in [93] comes predomi-

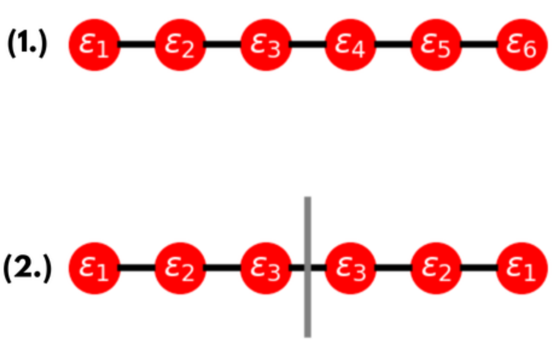

Figure 4.1: The mutation process illustrated for a 6-site chain. The initial randomised chain (1.) is reflected about its centre (2.) from the left, to enforce mirror symmetry of the on-site energies throughout the execution of the algorithm. The solid black lines connecting the sites imply homogeneous coupling $J_{i,i+1} = 1$.

nantly through the aforementioned mirroring-mutation process (See Fig.4.1) as well as the new fitness function. It is therefore suggested that the following results showcased in this thesis may be reasonably reproduced through simply making these modifications. Once the parameters are set within the fitness function, N may be adjusted through the scaling of the associated $N \times N$ Hamiltonian matrix, along with the size of the initial and final states (Eq.(2.10)). The value of p was increased in even-integer steps (to the next odd integer) within Eq.(4.2) to further produce solutions for very high-fidelity transfer with the desired spectral characteristics.

4.2 Persymmetric Matrix Reconstruction

To find the diagonal and off-diagonal terms of a tridiagonal mirror-symmetric matrix, with only the knowledge of the relative spacing of its eiegenvalues, one may also employ an inverse eigenvalue method. For the persymmetric matrix reconstruction work presented in this thesis, I wrote code that was informed by the theoretical principles and algorithms outlined in the references provided within this chapter. This code (See Appendix.A for the full implementation within Python) was useful in enabling the analysis of protocols (and comparisons between multiple) carried out in this research.

4.2.1 Mathematical Foundation

Since the late 70's, it has been a matter of interest amongst mathematicians to establish numerical methods/algorithms to reconstruct Jacobi matrices (positive, semi-definite and tridiagonal with negative co-diagonal elements) from their corresponding spectral data [97, 98, 99, 100, 101]. Particularly, a Jacobi matrix, H, of a specific kind, known as *persymmetric* (or mirror-symmetric for our purposes) offers advantages due to the incident simplification in computation resulting from the uniform condition of Eq.(3.4)

$$\begin{aligned} H &= \begin{pmatrix} \varepsilon_1 & J_{1,2} & \cdots & 0 & 0 \\ J_{1,2} & \varepsilon_2 & \cdots & 0 & 0 \\ \vdots & \vdots & \ddots & \vdots & \vdots \\ 0 & 0 & \cdots & \varepsilon_{N-1} & J_{N-1,N} \\ 0 & 0 & \cdots & J_{N-1,N} & \varepsilon_N \end{pmatrix} \\ &= \begin{pmatrix} \varepsilon_N & J_{N-1,N} & \cdots & 0 & 0 \\ J_{N-1,N} & \varepsilon_{N-1} & \cdots & 0 & 0 \\ \vdots & \vdots & \ddots & \vdots & \vdots \\ 0 & 0 & \cdots & \varepsilon_2 & J_{1,2} \\ 0 & 0 & \cdots & J_{1,2} & \varepsilon_1 \end{pmatrix}. \end{aligned} \tag{4.4}$$

Calculating the matrix elements of matrices of the kind presented in Eq.(4.4), from their spectra, is the essence of an inverse eigenvalue problem [100, 101].

There are a number of established approaches (algorithms) which manipulate monic-orthogonal polynomials, the weights characterized by their discrete inner product, and three-term recurrence relations to yield a numerically stable, and *unique* persymmetric matrix [97, 98, 99].

Let $P_N(\lambda) = \prod_{k=1}^{N}(\lambda - \lambda_k)$ represent the characteristic polynomial of H, with the jth leading principal minor of the matrix $(\lambda I - H_N)$, denoted by $P_j(\lambda)$, representing the characteristic polynomial of truncated (starting from the upper left corner) H. The sequence of polynomials $P_j(\lambda)$ forms a Sturm sequence, satisfying a three-term recurrence relation for $j = 1, 2, \ldots, N$

$$P_j(\lambda) = (\lambda - \epsilon_j)P_{j-1}(\lambda) - J_{j-1}^2 P_{j-2}(\lambda). \tag{4.5}$$

A Sturm sequence, by definition, exhibits a crucial property, in that the roots of $P_j(\lambda)$, denoted as λ_{jk}, interlace those of $P_{j-1}(\lambda)$

$$\lambda_{j,j-1} < \lambda_{j-1,j-2} < \lambda_{j,j-2} < \cdots < \lambda_{j,1} < \lambda_{j-1,0} < \lambda_{j,0}. \tag{4.6}$$

This property leads to the following relationship [40]

$$\mathrm{sgn}[P_{N-1}(\lambda_k)] = (-1) \times \mathrm{sgn}[P_{N-1}(\lambda_{k-1})],$$

which serves as mathematical foundation of the alternating parity of the eigenvectors, as these polynomials are related to the coefficients within the eigenbasis expansion. Using a combined approach, only requiring knowledge of the spacing of the spectral data to calculate the weights [98, 99]

$$w_k = \prod_{j \neq k}^{N-1} \frac{1}{|\lambda_k - \lambda_j|},$$

which are defined with respect to orthogonal polynomials discrete inner products via

$$\langle f, g \rangle = \sum_{k=1}^{N} f(\lambda_k) g(\lambda_k) w_k,$$

where $f(\lambda_k)$ and $g(\lambda_k)$ are generic monic-orthogonal polynomials, we may capitalize on the three-term recurrence relation and interlacing property of the roots of the polynomials (Eq.(4.6)) to deduce the entries of the tridiagonal matrix. Note, two polynomials are said to be orthogonal with respect to the weights w_k, which measures the contribution of specific eigenvalues to their inner product.

4.2.2 Calculating Matrix Elements from Spectral Data

We may use the recurrence relation (Eq.(4.5)) and initially set P_0 to 1, and P_1 to $\lambda - \lambda_1$, where λ_1 is one of the eigenvalues of H_N, to find the coupling and on-site potentials governed by $\lambda_k \in \{\lambda_1, \lambda_2, \ldots, \lambda_N\}$

$$\epsilon_{i-1} = \frac{\langle \lambda \cdot P_{i-1,:}, P_{i-1,:} \rangle}{\|P_{i-1,:}\|^2} = \frac{\sum_{k=0}^{N} \lambda_k \cdot P_{i-1}(\lambda_k)^2 \cdot w_k}{\sum_{k=0}^{n-1} P_{i-1}(\lambda_k)^2 \cdot w_k}, \tag{4.7}$$

$$J_{i-1} = \frac{\|P_{i,:}\|}{\|P_{i-1,:}\|} = \frac{\sum_{k=1}^{N} P_i(\lambda_k)^2 \cdot w_k}{\sum_{k=1}^{N} P_{i-1}(\lambda_k)^2 \cdot w_k}, \tag{4.8}$$

iterating over λ_k [101]. The polynomials evaluated at each eigenvalue $P_i(\lambda_k)$, which satisfy Eq.(4.5), and the weights w_k, maintains accurate representation of the spectral structure within the reconstruction [98]. Through this numerically stable approach, one may reconstruct all of the elements of a tridiagonal persymmetric matrix (Eq.(4.4)), with knowledge only of the relative spectral spacing. The utility of this method, from the standpoint of constructing quantum communication protocols, seems to have been first discussed by Yung and Bose [40], followed by Vinet and Kay [70, 89].

5

Results and Discussion

In the following section, we outline the results from the genetic algorithm designed for on-site energy parametrization, as presented in Sec.4.1. Any reference to time within the figures shown, proceeds through the use of natural units ($\hbar = 1$), consequently making J_{max} the characteristic energy/inverse time scale.

5.1 Results from Tailored Genetic Algorithm

5.1.1 $N = 3$-site chain

Beginning with a 3-site chain, using $A = 1.0$ and $B = 1.0$ from Eq.(4.3), as a test, the genetic algorithm was able to obtain the predicted relative values of the on-site energies for $p = 3 - 11$. Consequently, the highlighted points within Fig.5.1 display perfect correspondence between analytical foundation (Eq.(3.22)) and numerical findings. Furthermore, the dynamics for each of the p-solutions for $N = 3$ are shown in Fig.5.2, where the increase in time required for successful state transfer is in accordance with Eq.(3.20). The distinct shapes associated with the fidelity of the evolved and initial state over time, are formed by the number of 'attempts' (we may denote as a) required for the state to mirror invert completely

$$a = \frac{(p-1)}{2}.$$

Clearly for $p = 1$ no previous attempts are required, making this the most time-efficient approach to PST. The next best option is waiting proportionally to p, for the next opportunity.

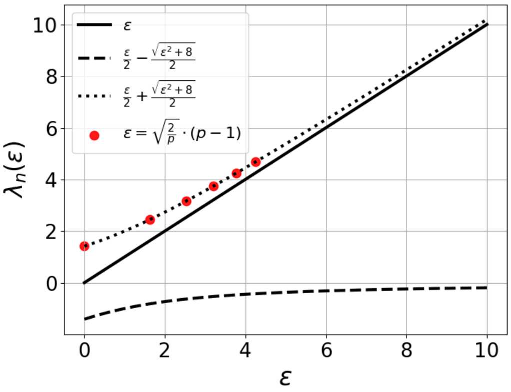

Figure 5.1: Eigenvalue equations for $N = 3$, (with central on-site energy set to zero) plotted as a function of ε, the two outer on-site energies, with the corresponding values of the on-site energies from the numerical results. The highlighted (red) points correspond to the values of epsilon (Eq.(3.22)) that the spacing between the top two eigenvalues and the lowest two eigenvalues are exactly; $p = 1 - 11$ (increasing by successive odd integers at each step).

5.1.2 $N = 4; p = 3$ and $N = 7; p = 5$

As will be demonstrated, we have discovered families of solutions for different p and N. We start by discussing two specific examples. Here, we present two distinct N-site: p-solutions, for both even ($N = 4$) and odd ($N = 7$) site chains, from a tailored genetic algorithm approach to grant QPST. Optimizing first the $N = 4$-site chain, in setting $A = 1.0$ and $B = 0.5$ within Eq.(4.3), we observe from Fig.5.3(a) that the optimized protocol follows a positive parabolic structure, about the centre of the chain, similar to the inverted triangular configuration showcased by the $N = 3$ analytical case (Eq.(3.21)). This solution, founded by a $p = 3$ spacing of the eigenvalues (Fig.5.3(c)), will transfer encoded information across the chain with a fidelity of 99.99% (Fig.5.3(a)).

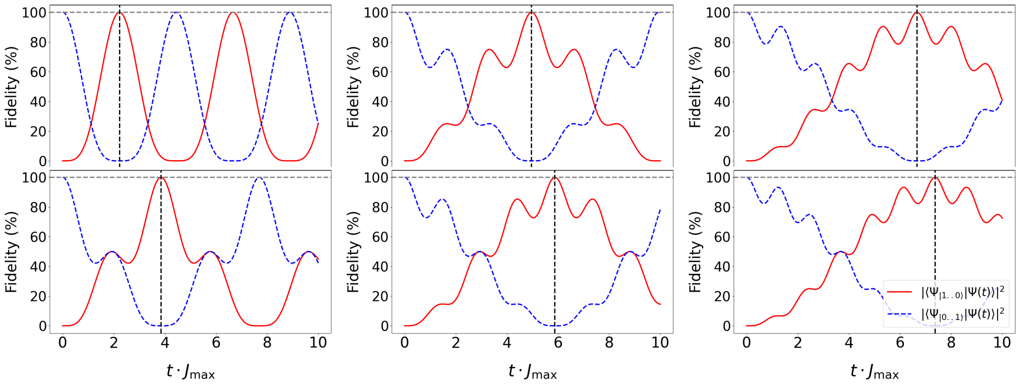

Figure 5.2: Fidelity with target state (red solid curve) and Fidelity with initial state (blue dashed curve) versus re-scaled time $t \cdot J_{max}$ for $p = 1$ (top left) to 11 (bottom right), for $N = 3$-site chain. The figures are displayed corresponding to the top row being $p = 1, 5, 7$ and bottom row $p = 3, 9, 11$. The dashed (grey) horizontal line provides a reference line along fidelity value of 100% and the dashed (black) vertical line indicates first instance of perfect state transfer.

.

Then in leveraging the genetic algorithm approach for $N = 7$-sites, $A = 1.0$ and $B = 0.1$ (relaxing spectral optimization), with an auxiliary search for $p = 5$ spacing, we observe that the positive parabolic structure of the on-site energies is also maintained in an odd-site chain (Fig.5.4), with transfer fidelity percentages that compare favorably to those of the previously-known coupling protocols in Sec.3.3.1. It was previously established that perfect state transfer (PST) is possible in homogeneously coupled chains of size $N = 3$ [44]. While this configuration for an N-site chain ($N = 7$) does not achieve PST, it demonstrates that even in a chain more than double the size of $N = 3$, high transfer fidelity ($\approx 99\%$, see Fig.5.4(b)) can still be attained.

5.1.3 Families of p-solutions

In extending the application of the genetic algorithm to a number of N-sites, we discovered a set of optimal solutions characterized by specific p-values (3, 5, and 7) across various chain lengths ($N = 3$ to 7), as depicted

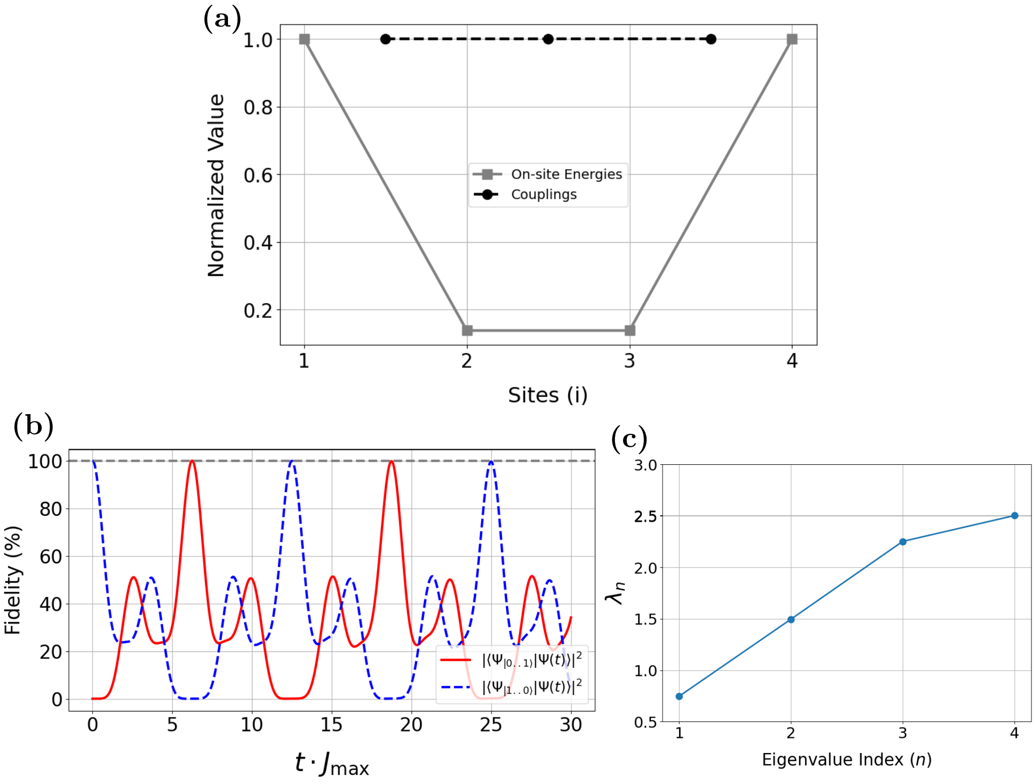

Figure 5.3: On-site energies and coupling configuration across the optimized $N = 4$-site chain (a). $N = 4$; $p = 3$-solution associated transfer dynamics (b) and spectrum (c). Transfer fidelity of 99.99% at time $t \cdot J_{\text{max}}$= 6.28. The eigenvalue magnitudes λ_n (along the y-axis of (c)) have been rounded to 2 significant figures for convenience. The 'Normalized Value' on the y-axis of (a) is calculated as $(\frac{\varepsilon_i}{\varepsilon_{max}})$.

in Fig.5.5. The p-solutions for different chain lengths can be grouped into distinct families, with respect to the time required for PST (for $N = 3$) and QPST (for $N = 4$ to 7). Each individual p-family exhibits an approximately linear dependence on the chain length N and of the transfer time in units of $t \cdot J_{max}$, with a gradient that increases with increasing p. The on-site energy configuration trends for these different p-solutions are displayed in Fig.5.6. The trends showcase an approximate parabolicity of the on-site energies about the centre of the chain, similar to the analytical results of

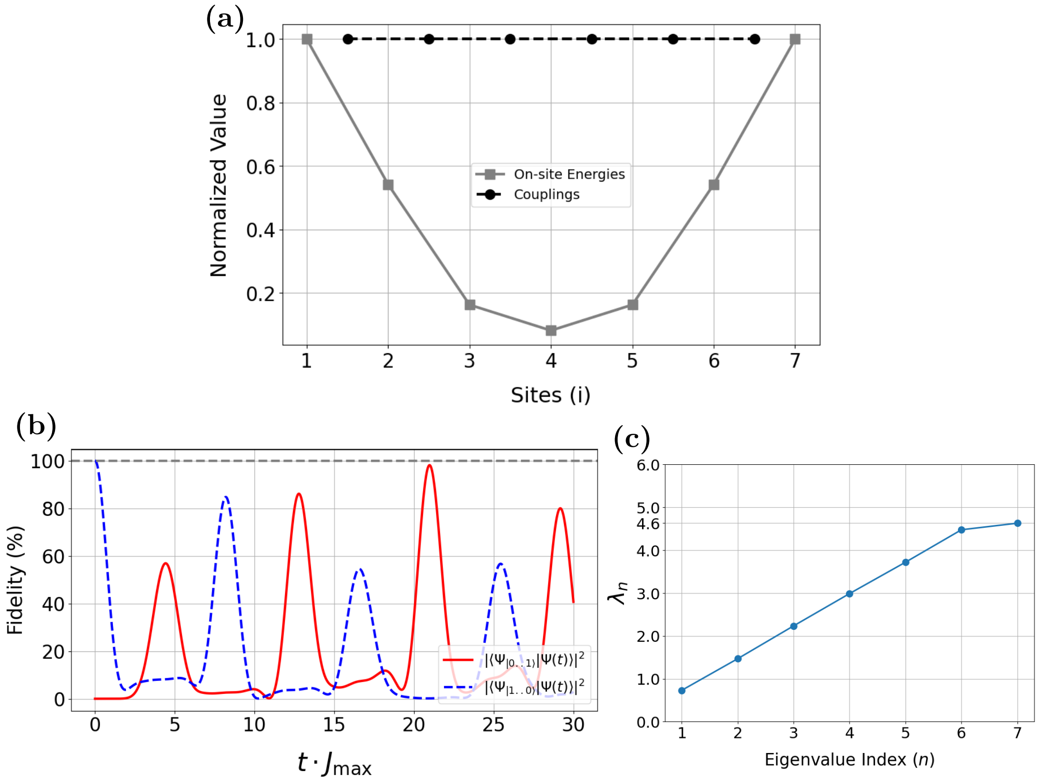

Figure 5.4: On-site energies and coupling configuration across the optimized $N = 7$-site chain (a). $N = 7$; $p = 5$-solution associated transfer dynamics (b) and spectrum (c). Transfer fidelity of 98.52% at time $t \cdot J_{\mathrm{max}}$=20.97. The eigenvalue magnitudes λ_n (along the y-axis of (c)) have been rounded to 2 significant figures for convenience. The 'Normalized Value' on the y-axis of (a) is calculated as $(\frac{\varepsilon_i}{\varepsilon_{max}})$.

the $N = 3$-site chain, with the inverted triangular configuration (Eq.(3.21)). Furthermore, the degree of steepness of the descent from the two outer on-site energies towards the middle, generally becomes larger with increasing order of p. The general shape and structure of the spectra associated with various strengths of pinching between the highest and second highest eigenvalue, can be observed in these two eigenvalues tending towards degeneracy as p increases.

The genetic algorithm was also able to find other p-solutions for $N > 7$,

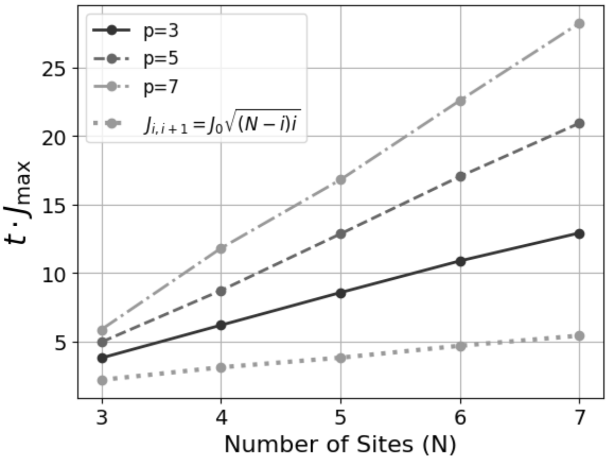

Figure 5.5: Comparison of times (in units of $t \cdot J_{max}$) to acquire QPST (PST for $N = 3$) via the on-site energy parametrization, and the previously known coupling scheme with no on-site energy variation (Eq.(3.19)).

such as $N = 8$ and $N = 9$ (not shown), but it becomes progressively more difficult to systematically extend the complete range of families, of the kind exhibited in Fig.5.5, for larger N.

5.2 QPST vs. PST

Within this section we outline the nuances of different classification schemes pertaining to state transfer protocols and the necessary trade-offs therein. In general, one can conclude that PST has not occurred if the initial state $|\psi_1\rangle$ has not fully transitioned to $|\psi_N\rangle$. Therefore, regarding the transfer fidelity over $t \in \mathbb{R}^+$, there is a quantity κ such that

$$|\langle\psi_N|U(t_m^*, 0)|\psi_1\rangle|^2 = 1 - \kappa, \quad \text{where} \quad 0 < \kappa \leq 1. \tag{5.1}$$

Here, t_m^* is the time in which the transfer fidelity is maximal. This is a sufficient argument due to the defining property of PST (Eq.(2.13)) being a transfer fidelity of unity with periodicity (Eq.(3.14)). There are more so-

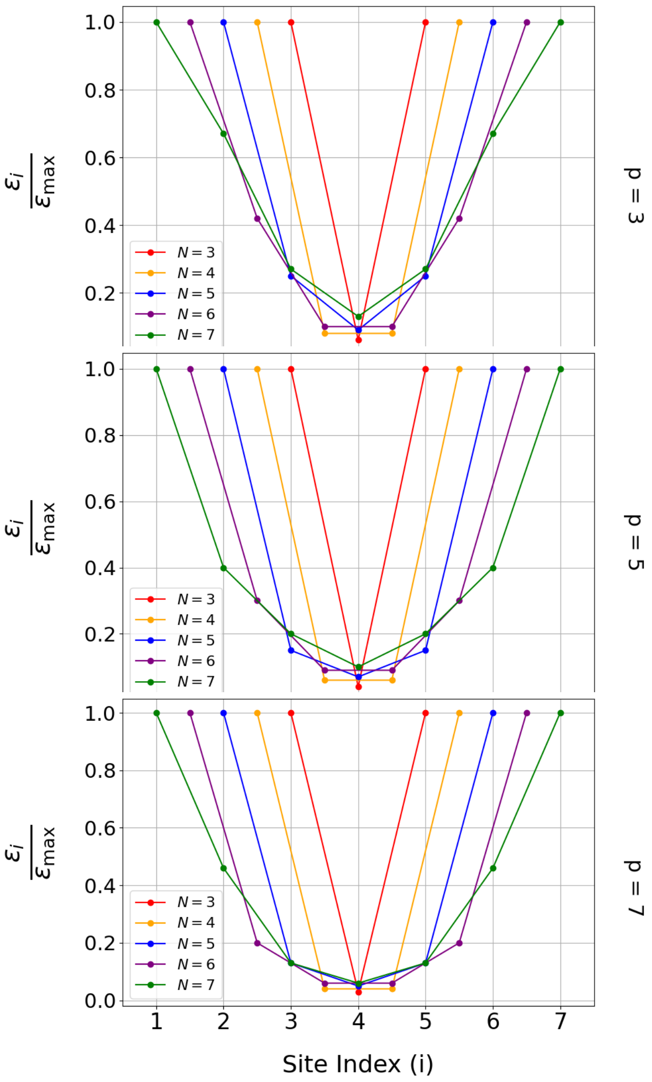

Figure 5.6: On-site configuration trends for $N = 1 - 7$ spin chains, considering p-values of 3, 5, and 7 for the solution families. Each plotted point is shifted for $N < 7$ along the x-axis by $(7-N)-\frac{1}{2}$, aligning each plot's central site/mid-bond center with the midpoint of $N = 7$. This adjustment enables a more convenient comparison of the relative strengths of outer-onsite energies versus central site potentials across different chain lengths and solution families.

phisticated theorems and conditions although, regarding the codification of 'pretty good state transfer' or PGST [72, 73, 102]. Namely, for homogeneously coupled graphs (chains) governed by an XY Hamiltonian, with unweighted vertices (on-site energies ignored $\varepsilon_i = 0$, for all i), the associated quantum walk may exhibit PGST if the total number of vertices (N-sites) is equal to $q - 1$, where q is a prime integer [102]. The family of solutions we have shown here exhibit transfer fidelities between 99.9% and 90.2% (corresponding to $0.01 < \kappa \leq 0.1$, within Eq.(5.1)), as shown in Table.5.1. They do not also exhibit perfect periodicity (particularly within longer time frames, see Fig.5.8). Hence, we feel it more appropriate to associate them within the previously established, more flexible category of high-fidelity solutions in QPST [103].

As an illustrative example of the discrepancies between PST and QPST, we may begin with a previously discovered, optimized high-fidelity solution of a 5-site chain with a mostly equidistant then 'pinched' ($p = 3$) spectra

$$H_{XY} = \begin{pmatrix} 3.4000 & 0.9100 & 0.000 & 0.000 & 0.000 \\ 0.9100 & 2.6000 & 0.9100 & 0.000 & 0.000 \\ 0.000 & 0.9100 & 2.3333 & 0.9100 & 0.000 \\ 0.000 & 0.000 & 0.9100 & 2.6000 & 0.9100 \\ 0.000 & 0.000 & 0.000 & 0.9100 & 3.4000 \end{pmatrix} \tag{5.2}$$

where we have found all of the matrix elements $\langle i|H_{ij}|j\rangle$ of Eq.(2.3) via genetic algorithm optimization. However we have now simply set $J_{i,i+1} = 0.91$ for future convenience. From Fig.5.7 we can see firstly that though this is a completely homogeneously coupled system we have described in Eq.(5.2), we have shown transfer fidelity of 99.98% within the time window presented. Through direct diagonalization of the matrix Eq.(5.2), the associated spectra which dictates the transfer efficacy throughout the time evolution of the state can be shown to *nearly* but not precisely satisfy the conditions on the eigenvalues (Eq.(3.17))

$$\lambda_{N=5} \in \{1.006, 2.006, 3.001, 3.994, 4.326\},$$

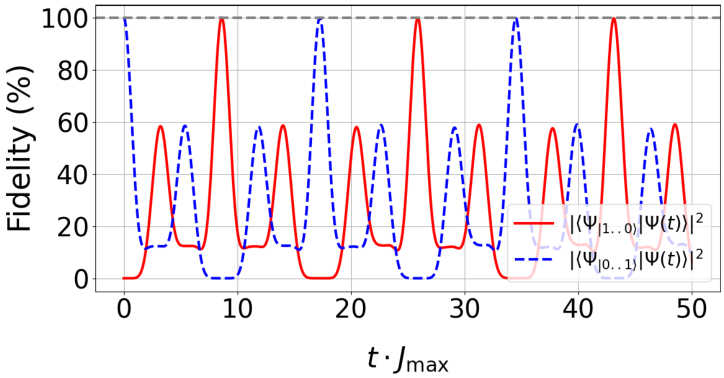

Figure 5.7: High-fidelity dynamics plot of N = 5 with a pinch between the highest two eigenvalues of exactly $\frac{1}{3}$ of the differences of each other eigenvalue pair. Highest fidelity attained: 99.98% at $t \cdot J_{max} = 8.63$. Modest decay exemplified by each subsequent 'quasi-mirroring' attempt (2nd and 3rd peak of 99.84% and 99.56% at $t \cdot J_{max} = 25.89$ and 43.15 respectively).

and therefore the periodicity of $F(t) \approx 100\%$ over arbitrarily long time scales, characteristic to PST solutions, cannot be expected. We may however use the inverse eigenvalue method (discussed in Sec.4.2) to reconstruct the unique persymmetric matrix which fulfills the conditions concretely, by using the spectral points

$$\lambda^*_{N=5} \in \left\{1.00, 2.00, 3.00, 4.00, 4.3\overline{3}\right\}, \tag{5.3}$$

and subsequently find the solution for the system capable of PST to be

$$H^*_{XY} = \begin{pmatrix} 3.400 & 0.9165 & 0.000 & 0.000 & 0.000 \\ 0.9165 & 2.600 & 0.9129 & 0.000 & 0.000 \\ 0.000 & 0.9129 & 2.333 & 0.9129 & 0.000 \\ 0.000 & 0.000 & 0.9129 & 2.600 & 0.9165 \\ 0.000 & 0.000 & 0.000 & 0.9165 & 3.400 \end{pmatrix}, \tag{5.4}$$

which may be subsequently diagonlized to regain the spectrum Eq.(5.3) and thereby observe the success of the numerical reconstruction. Though not completely homogeneous, and therefore capitalizing on the apparent advantages of such solutions, the difference in the energies of the coupling required to transition from QPST to PST is just 0.4%. Comparing this to the well-known coupling model in Eq.(3.19), which for a 5-site chain with initial strength $J_0 = 0.91$, this requires a difference of $\approx 20\%$ between the maximum and minimum coupling values for PST to occur.

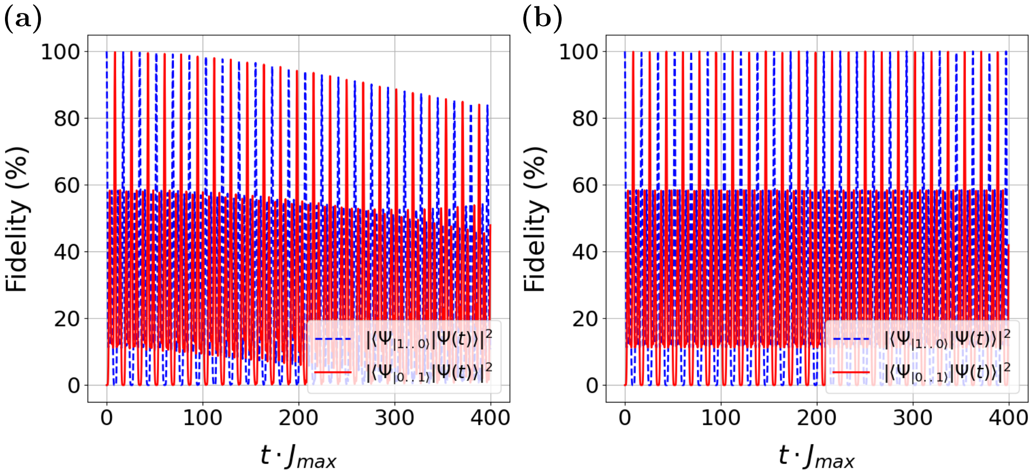

Figure 5.8: Comparison of the transfer fidelity over a significantly longer time frame than what we have considered before ($t \cdot J_{max} = 400$), between an optimized QPST solution (a) and a PST (b) solution derived from persymmetric matrix reconstruction.

In discussing the trade-offs between the QPST and PST solutions in this example, the transfer fidelity decay over extended time periods, which is characteristic of QPST, as shown in Fig.5.8(a), may be problematic if the system is expected to perform multiple mirror inversions over time. In the case where our system is being used to cache information, such as for short-term memory storage, multiple mirror inversions are crucial in order to transport the information spatially to the opposite end of the chain, return back, and be able to be retrieved again (if desired) at the injection site ($i = 1$), at predictable time intervals of $l \cdot t_m$ (where l is an even integer). We can see from the comparison within Fig.5.8, that not only does the transfer fidelity score (red-solid line) decay over an extended time frame for the QPST protocol, but so does the fidelity between the evolved and fixed initial state (blue-dotted line), thereby curtailing its relative storage capabilities and presenting a clear advantage for PST protocols. For this particular $N = 5$-site solution, if the system only needs to perform a mirror inversion once (or even a couple of attempts with high transfer fidelity), the difference in transfer fidelities between QPST and PST protocols is minimal. Therefore, for a 'single-shot' transfer of information, which may be all that is required of linear registers within modular ensembles, either protocol will effectively achieve the desired outcome in this case.

Within the next section, we discuss the gate operation times in relation to being orders of magnitude smaller than the best estimates for the time for the system decohere, as an advantage consistent with Di Vincenzo's third criteria (Sec.1.2.3). However, regarding the prospective necessity for a single mirror inversion, if the number of gate operations are of the order of $\gg 1$, this may prove to be superfluous as the primary concern would be the fidelity value at the first peak.

5.3 Experimental Considerations

In this section we outline the importance in reconciling theoretical exploration of the homogeneously-coupled quantum communication protocols with experimental realizablity and practicality.

5.3.1 Robustness

The fidelities associated with the on-site energy trends displayed in Fig.5.6 may be found in Table.5.1. This table presents, in the far left column, the number of sites $N_{(p=1-7)}$, sub-scripted with the corresponding p-value for the solution, and includes the degree of precision required for the values of ε_i

to enable QPST. Notably, all of the fidelity measurements displayed within Table.5.1, even when rounded to one significant figure, comfortably exceed $66.6\overline{6}\%$ (discussed in Sec.2.4). This demonstrates a level of robustness to imprecision which still allows for high fidelity transfer, even though rounding each on-site energy value to one significant figure results in a noticeably different structure of the on-site energies across the chain (See Fig.5.9). The

$N_{(p=3)}$	**4 s.f.**	**3 s.f.**	**2 s.f.**	**1 s.f.**
4	99.9%	99.9%	99.8%	98.8%
5	99.9%	99.9%	99.9%	97.7%
6	99.8%	99.8%	99.4%	97.1%
7	96.7%	96.7%	95.6%	94.1%
$N_{(p=5)}$	**4 s.f.**	**3 s.f.**	**2 s.f.**	**1 s.f.**
4	99.9%	99.9%	99.8%	98.4%
5	99.5%	99.5%	98.0%	90.3%
6	97.8%	97.8%	97.4%	89.2%
7	98.5%	98.5%	94.1%	87.9%
$N_{(p=7)}$	**4 s.f.**	**3 s.f.**	**2 s.f.**	**1 s.f.**
4	99.7%	99.6%	99.4%	98.1%
5	98.7%	98.7%	92.2%	91.5%
6	94.6%	94.6%	90.7%	89.8%
7	90.2%	90.2%	82.2%	81.1%

Table 5.1: Transfer fidelity scores associated with the presented on-site energy configurations, with decreasing levels of precision, quantified by the reduction in the number of significant figures of, ε_i. This table demonstrates the robustness of the configurations shown for $p = 3-7$ within Fig.5.6, for N-site chains ranging from 4 to 7 sites, evaluated up to 1 significant figure as a metric for the degree of experimental precision required.

reduction in significant figures involves a different approach to that employed within [93], as it involves rounding numbers in the conventional sense, as opposed to a hard ‘cut’ without arithmetic rounding. As an illustration, the value 1.452, containing four significant figures (4 s.f.), is rounded to 1.45 when expressed to three significant figures (3 s.f.), 1.5 rounded to two significant figures (2 s.f.), and finally 2 when reduced to one significant figure (1 s.f.).

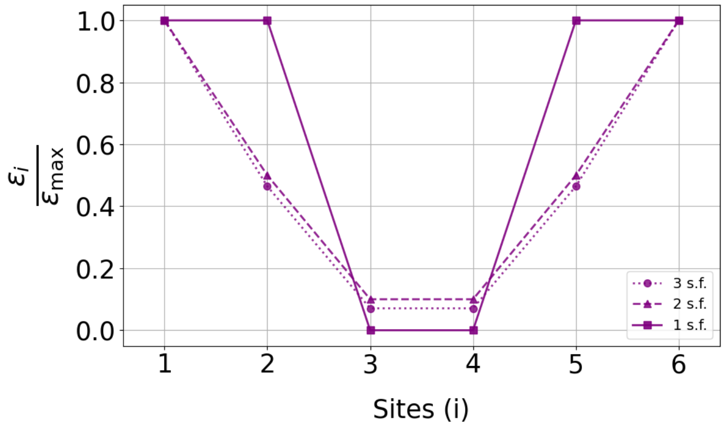

Figure 5.9: On-site configuration trend for $N = 6$; $p = 3$ chain with decreasing orders of precision. When the values of ε_i is rounded to 1 significant figure (solid line-square marker), 97.1% fidelity is still achieved (Table.5.1). The plot for 4 s.f. was simply omitted due to the respective plots associated with 4 s.f. and 3 s.f. overlapping due to the degree of similarity of the values, obstructing visual differentiation.

This approach provides another way to test the system's parameter error tolerance, offering further insight into the reproducibility of these protocols within potentially non-ideal settings.

5.3.2 Hardware Realizability

As J_{max} is hardware-dependent and the times to achieve QPST occur within a time window of approximately $t \cdot J_{max} = 30$ (See Fig.5.5), we may now produce a qualitative analysis observing how these protocols may be effectively incorporated within physical hardware. In reference to DiVincenzo's third requirement, Sec.1.2.3, for a physically realizable quantum computer [15], we must ensure that

$$\frac{T_2}{T_{QPST}} \gg 1, \tag{5.5}$$

and therefore that our time to QPST is much less than the coherence time T_2, in which the system is likely to decohere. In defining T_{QPST} as the time (in seconds) required for QPST, we need only to observe the characteristic energy values intrinsic to candidate hardware environments [31, 64].

Table.5.2 demonstrates (in the number of operations, measured by the ratio $(\frac{T_2}{T_{QPST}})$) that our protocol fulfills the criteria (Eq.(5.5)), in allowing for a substantial number of operations/computational attempts before concerns related to decoherence become relevant.

Hardware	$\mathbf{J_{max}}/\hbar$	$\mathbf{T}_{\text{QPST}}$	$\mathbf{T_2}$	$(\mathbf{T_2}/\mathbf{T}_{\text{QPST}})$
Superconductor [64]	10 GHz	3 ns	50 μs	$\sim 10^4$
Ion Trap [31]	150 MHz	0.2 μs	$\sim$ minutes	$\sim 10^7$
Semiconductor (Si-SiGe) [31]	10 MHz	3 μs	100 μs	$\sim 10^1$
Neutral Atom Array [31]	1 MHz	30 μs	1 second	$\sim 10^4$

Table 5.2: Comparison of different hardware in terms of operation time against decoherence. J_{max} corresponds to the typical energy scale estimate derived from the typical two-qubit gate operation time τ_2, and T_{QPST} is the estimated time (in seconds) required for QPST. The Si-SiGe semiconductor was selected specifically as it allows for control over the largest number (to-date) of individually controlled semiconducting spin-qubits ($N = 6$).

All barring the semiconductor hardware allows for multiple orders of magnitude of operations, within the frame of time considered. In reflecting that T_{QPST} was taken simply as the largest time considered within Fig.5.5, the specific times (in seconds) associated with the various number of sites (p-solutions) will be able to operate even longer. It is because of this reasoning that the number of attempts calculated from Eq.(5.5), and the values taken from Table.5.2, may be understood as a lower limit. This strongly indicates that our proposals could be utilized effectively within a variety of different physical hardware, for which the evolution of the system is governed by a Hamiltonian of the form Eq.(2.3).

6

Conclusions and Future Work

6.1 Conclusions

To conclude, we have demonstrated through the use of a genetic algorithm, that novel solutions in the configurations of on-site energies within a range of uniformly coupled XY Hamiltonians may be shown to yield QPST. These optimized solutions are in perfect correspondence with the analytical description of chains of the length of $N = 3$, also displayed here, and have a unique spectrum in comparison to previously-established coupling configurations, for which PST is expected. The general structure and approach for previous genetic algorithm investigations of spin chains/networks was maintained in this work, with only modest changes being made to the fitness function and mutation process.

This choice ensures reproducibility and consistency with pre-established methodologies, thereby facilitating comparison and validation of results across analyses. Alternative numerical approaches such as persymmetric matrix reconstruction can also be used to find PST protocols through rounding of the optimized spectra, to the spectra corresponding to necessary spectral conditions for PST, as a QPST-to-PST transition process. Using both in tandem can unearth a potential for synergy between theoretical novelty and experimental realizability. We also present that these protocols are robust to uncertainty/imprecision in the approximations of the on-site energies ε_i, across the chains through which we aim to transmit and/or store encoded information.

In paraphrasing Scott Aaronson [104], due to pioneering work in the 90's (quantum error correction/fault-tolerance) we have realized what we are up against is *merely* an incredibly difficult engineering problem. It may suffice to say we are standing at a pivotal point within history in pushing the boundaries of what was previously thought to be an impossible engineering project, and therefore we cannot afford any potential avenue for innovation to be left without meticulous scrutiny. It is through theoretical explorations such as these, along with future collaborations with experimentalists, that mankind may eventually be beholden to the age of emphatic quantum advantage.

6.2 Future work

Current and future research endeavours are focusing on extending the optimization and numerical techniques employed herein to explore larger N-site chains, as it may be advantageous to use linear registers of the order of $\sim 10^2$ qubits. A complementary approach involving unitary transformations [105] could also be used to explore more complex (non-linear) networks. Furthermore, there is an opportunity to investigate the physical foundations underlying the observed on-site energy configuration patterns, particularly in the parabolic orientation evident in configurations with $p > 1$. There is also an underdeveloped area in exploring the relation between temperature and information transfer protocols, as often is the case that numerical simulations within this area are conducted within the zero-temperature regime. Ongoing efforts by the York research group are currently exploring these questions, though a detailed discussion lies beyond the scope of this thesis. We suggest that these initiatives deepen our understanding of the technological potential within quantum systems and provide additional insights into experimental proposals to improve upon current quantum communication protocols.

Appendices

A

Python Code: Persymmetric Matrix Reconstruction

The following Python code simulates quantum state transfer in a linear chain of N-sites, using monic orthogonal polynomials and relative spectral weights w_k (theory discussed in Sec.4.2) to construct a persymmetric matrix [97, 98, 101], which is then implemented into the time evolution of the system, via $\hat{U} = e^{-iHt}$ ($\hbar = 1$). The code is defaulted to 6 eigenvalues (thereby instating an $N = 6$-site chain), with an eigenvalue spacing consistent with $p = 5$.

```python
import numpy as np
import matplotlib.pyplot as plt
from scipy.linalg import expm

# Set the number of and values of the spectrum and consequently the length of the chain N
eigenvalues = np.array([1, 2, 3, 4, 5, 5.2])
N = len(eigenvalues)

# Function to compute weights and orthogonal polynomials
def compute_weights_and_orthogonal_polynomials(eigenvalues):
    n = len(eigenvalues)
    e = np.zeros(n)  # On-site energies
    J = np.zeros(n-1)  # Coupling terms
    p = np.zeros((n, n))  # Orthogonal polynomials
    H = np.zeros((n, n))  # Hamiltonian matrix
    w = np.ones(n)  # Weights

    # Compute weights
```

```python
    for k in range(n):
        for j in range(n):
            if j != k:
                w[k] /= abs(eigenvalues[k] - eigenvalues[j])

    # Compute orthogonal polynomials
    p[0, :] = 1
    e[0] = np.sum(eigenvalues * p[0, :]**2 * w) / np.sum(p[0, :]**2 * w)
    p[1, :] = (eigenvalues - e[0]) * p[0, :]
    J[0] = np.sum(p[1, :]**2 * w) / np.sum(p[0, :]**2 * w)

    # The calculation of the matrix elements
    for i in range(2, n):
        e[i-1] = np.sum(eigenvalues * p[i-1, :]**2 * w) / np.sum(p[i-1, :]**2 * w)
        p[i, :] = (eigenvalues - e[i-1]) * p[i-1, :] - J[i-2] * p[i-2, :]
        J[i-1] = np.sum(p[i, :]**2 * w) / np.sum(p[i-1, :]**2 * w)

    # Constructing the unique persymmetric matrix
    for i in range(n):
        H[i, i] = e[i]
        if i < n-1:
            H[i, i+1] = np.sqrt(J[i])
            H[i+1, i] = np.sqrt(J[i])

    return w, H

# Calculate weights and Hamiltonian matrix
weights, H = compute_weights_and_orthogonal_polynomials(eigenvalues)

# Print the unique persymmetric matrix
np.set_printoptions(edgeitems=30, linewidth=150, formatter=dict(float=lambda x: "%.5f" % x))
print(’H:’)
print(H)

# Define fidelity function
def fidelity(initial_state, target_state):
    return np.abs(np.vdot(initial_state, target_state))**2

# Define initial state (excitation at the beginning of the chain)
initial_state = np.zeros(len(eigenvalues))
initial_state[0] = 1

```

```
# Define target state (excitation at the other end of the chain)
target_state = np.zeros(len(eigenvalues))
target_state[-1] = 1

# Define time points
t_values = np.linspace(0, N*np.pi, 2000)  # Time period

# Initialize lists to store fidelity values
initial_fidelity_values = []
target_fidelity_values = []
highest_fidelity = 0

# Loop over time points to calculate fidelity
for t in t_values:
    # Time evolution operator
    U = expm(-H/(np.max(np.diagonal(H, -1))) * 1j * t)

    # Apply time evolution to the initial state
    evolved_state = U.dot(initial_state)

    # Calculate fidelity with initial state
    initial_fidelity = fidelity(initial_state, evolved_state)
    initial_fidelity_values.append(initial_fidelity)

    # Calculate fidelity with target state
    target_fidelity = fidelity(evolved_state, target_state)
    target_fidelity_values.append(target_fidelity)

    # Update highest fidelity and time at which it occurs
    highest_fidelity = max(highest_fidelity, target_fidelity)
    highest_fidelity_time = t_values[np.argmax(target_fidelity_values)]

# Plot transfer fidelity over time
plt.figure(figsize=(12, 6))

# Sort the eigenvalues and calculate difference between the highest two
sorted_eigenvalues = np.sort(eigenvalues)
difference = sorted_eigenvalues[-1] - sorted_eigenvalues[-2]

# Calculate p as the reciprocal of the difference
p = 1 / difference

# Plot the fidelities
```

```
plt.plot(t_values, initial_fidelity_values, 'b--', linewidth=2, label=r'$|\
    langle\Psi_{|1..0\rangle}|\Psi(t)\rangle|^2$')
plt.plot(t_values, target_fidelity_values, 'r-', linewidth=2, label=r'$|\
    langle\Psi_{|0..1\rangle}|\Psi(t)\rangle|^2$')
plt.xlabel('$t \cdot J_{max}$', labelpad=20, fontsize=15)
plt.ylabel('Fidelity', labelpad=20, fontsize=15)
plt.title(f'$N = {N};\\ p = {p:.1f}$', fontsize=15)
plt.legend(loc='lower right')
plt.grid(True)
plt.show()

# Print the highest fidelity attained and the corresponding time
print("Highest fidelity attained: {:.4%} at t = {:.2f}".format(
    highest_fidelity, highest_fidelity_time))
```

Listing A.1: Python code for persymmetric matrix reconstruction using spectral data. Subsuquent calculation and plot of transfer fidelity corresponding to the eigenvalues chosen.

References

[1] C. L. Degen, F. Reinhard, and P. Cappellaro. Quantum sensing. *Rev. Mod. Phys.*, 89:035002, Jul 2017.

[2] Kai Bongs, Simon Bennett, and Anke Lohmann. Quantum sensors will start a revolution. *Nature*, 617:672–675, 2023.

[3] Andrew D. Ludlow, Martin M. Boyd, Jun Ye, E. Peik, and P. O. Schmidt. Optical atomic clocks. *Rev. Mod. Phys.*, 87:637–701, Jun 2015.

[4] Vittorio Giovannetti, Seth Lloyd, and Lorenzo Maccone. Advances in quantum metrology. *Nature Photonics*, 5:222–229, 2011.

[5] Luca Pezzè, Augusto Smerzi, Markus K. Oberthaler, Roman Schmied, and Philipp Treutlein. Quantum metrology with nonclassical states of atomic ensembles. *Rev. Mod. Phys.*, 90:035005, Sep 2018.

[6] Nicolas Gisin and Rob Thew. Quantum communication. *Nature Photonics*, 1(3):165–171, 2007.

[7] Yu-Ao Chen, Qiang Zhang, Teng-Yun Chen, Wen-Qi Cai, Sheng-Kai Liao, Jun Zhang, Kai Chen, Juan Yin, Ji-Gang Ren, Zhu Chen, et al. An integrated space-to-ground quantum communication network over 4,600 kilometres. *Nature*, 589(7841):214–219, 2021.

[8] Román Orús, Samuel Mugel, and Enrique Lizaso. Quantum computing for finance: Overview and prospects. *Reviews in Physics*, 4:100028, 2019.

[9] M. Krelina. Quantum technology for military applications. *EPJ Quantum Technology*, 8:24, 2021.

[10] James A. Lewis and Georgia Wood. Quantum technology: Applications and implications. 2023. Center for Strategic and International Studies,Published on May 25, 2023.

[11] Jonathan Pritchard, Stephen Till, et al. Uk quantum technology landscape 2014. *Defence Science and Technology Laboratory, DSTL/PUB75620*, 2014.

[12] RC Yadav and MP Chaudhary. Racy nature—a sun technology towards quantum agriculture. *World*, 2(5):223–227, 2014.

[13] Peter Cooper, Philipp Ernst, Dieter Kiewell, and Dickon Pinner. Quantum computing just might save the planet. *McKinsey & Company*, 2022.

[14] John Preskill. Reliable quantum computers. *Proceedings of the Royal Society of London. Series A: Mathematical, Physical and Engineering Sciences*, 454:385–410, 1998.

[15] David P. DiVincenzo. The physical implementation of quantum computation. *Fortschritte der Physik*, 48(9–11):771–783, sep 2000.

[16] Sergio Boixo, Sergei V. Isakov, Vadim N. Smelyanskiy, and et al. Characterizing quantum supremacy in near-term devices. *Nature Physics*, 14:595–600, 2018.

[17] T. D. Ladd, F. Jelezko, R. Laflamme, Y. Nakamura, C. Monroe, and J. L. O'Brien. Quantum computers. *Nature*, 464(7285):45–53, 2010.

[18] Scott Aaronson and Lijie Chen. Complexity-theoretic foundations of quantum supremacy experiments, 2016. In: arXiv:1612.05903 [quant-ph].

[19] David Deutsch and Richard Jozsa. Rapid Solution of Problems by Quantum Computation. *Proceedings of the Royal Society of London Series A*, 439(1907):553–558, December 1992.

[20] Lov K. Grover. Quantum computers can search arbitrarily large databases by a single query. *Phys. Rev. Lett.*, 79:4709–4712, Dec 1997.

[21] P.W. Shor. Algorithms for quantum computation: discrete logarithms and factoring. pages 124–134, 1994.

[22] Jonathan P. Home, D. Hanneke, J. D. Jost, J. M. Amini, D. Leibfried, and D. J. Wineland. Complete methods set for scalable ion trap quantum information processing. *Science*, 325:1227–1230, 2009.

[23] Kae Nemoto, Michael Trupke, Simon J. Devitt, Ashley M. Stephens, Burkhard Scharfenberger, Kathrin Buczak, Tobias Nöbauer, Mark S. Everitt, Jörg Schmiedmayer, and William J. Munro. Photonic architecture for scalable quantum information processing in diamond. *Phys. Rev. X*, 4:031022, Aug 2014.

[24] K. Brown, J. Kim, and C. Monroe. Co-designing a scalable quantum computer with trapped atomic ions. *npj Quantum Information*, 2:16034, 2016.

[25] J. M. Gambetta, J. M. Chow, and M. Steffen. Building logical qubits in a superconducting quantum computing system. *npj Quantum Information*, 3:2, 2017.

[26] Koen Alexander et al. A manufacturable platform for photonic quantum computing, 2024. In: arXiv:2404.17570 [quant-ph].

[27] L. Li, L.D. Santis, I.B.W. Harris, et al. Heterogeneous integration of spin–photon interfaces with a cmos platform. *Nature*, 630:70–76, 2024.

[28] R. P. Feynman. Simulating physics with computers. *International Journal of Theoretical Physics*, 21(6):467–488, 1982.

[29] Dave Wecker, Matthew B. Hastings, Nathan Wiebe, Bryan K. Clark, Chetan Nayak, and Matthias Troyer. Solving strongly correlated electron models on a quantum computer. *Physical Review A*, 92(6), December 2015.

[30] A. L. Shaw, Z. Chen, J. Choi, et al. Benchmarking highly entangled states on a 60-atom analogue quantum simulator. *Nature*, 628:71–77, 2024.

[31] Bin Cheng, Xiu-Hao Deng, Xiu Gu, Yu He, Guangchong Hu, Peihao Huang, Jun Li, Ben-Chuan Lin, Dawei Lu, Yao Lu, Chudan Qiu, Hui Wang, Tao Xin, Shi Yu, Man-Hong Yung, Junkai Zeng, Song Zhang, Youpeng Zhong, Xinhua Peng, Franco Nori, and Dapeng Yu. Noisy intermediate-scale quantum computers. *Frontiers of Physics*, 18(2), March 2023.

[32] John Preskill. Quantum Computing in the NISQ era and beyond. *Quantum*, 2:79, August 2018.

[33] Earl T. Campbell, Barbara M. Terhal, and Christophe Vuillot. Roads towards fault-tolerant universal quantum computation. *Nature*, 549(7671):172–179, September 2017.

[34] Peter W. Shor. Fault-tolerant quantum computation, 1997. In: arXiv:quant-ph/9605011.

[35] Peter W. Shor. Scheme for reducing decoherence in quantum computer memory. *Phys. Rev. A*, 52:R2493–R2496, Oct 1995.

[36] Daniel Gottesman. An introduction to quantum error correction and fault-tolerant quantum computation, 2009. In: arXiv:0904.2557.

[37] Sougato Bose. Quantum communication through an unmodulated spin chain. *Phys. Rev. Lett.*, 91:207901, Nov 2003.

[38] Sougato Bose. Quantum communication through spin chain dynamics: an introductory overview. *Contemporary Physics*, 48(1):13–30, Jan 2007.

[39] G.M. Nikolopoulos and I. Jex. *Quantum State Transfer and Network Engineering*. Quantum Science and Technology. Springer Berlin Heidelberg, 2013.

[40] Man-Hong Yung and Sougato Bose. Perfect state transfer, effective gates, and entanglement generation in engineered bosonic and fermionic networks. *Phys. Rev. A*, 71:032310, Mar 2005.

[41] Marta P. Estarellas, Irene D'Amico, and Timothy P. Spiller. Robust quantum entanglement generation and generation-plus-storage protocols with spin chains. *Phys. Rev. A*, 95:042335, Apr 2017.

[42] Kieran N. Wilkinson, Marta P. Estarellas, T. Spiller, and I. D'Amico. Rapid and robust generation of einstein-podolsky-rosen pairs with spin chains. *Quantum Information and Computation*, 18(3-4):247–264, March 2018.

[43] Robert J. Chapman, Matteo Santandrea, Zixin Huang, Giacomo Corrielli, Andrea Crespi, Man-Hong Yung, Roberto Osellame, and Alberto Peruzzo. Experimental perfect state transfer of an entangled photonic qubit. *Nature Communications*, 7, 2016.

[44] M. Christandl, N. Datta, T. C. Dorlas, A. Ekert, A. Kay, and A. J. Landahl. Perfect transfer of arbitrary states in quantum spin networks. *Physical Review A*, 71(3):032312, March 2005.

[45] Georgios M Nikolopoulos, David Petrosyan, and P Lambropoulos. Electron wavepacket propagation in a chain of coupled quantum dots. *Journal of Physics: Condensed Matter*, 16(28):4991, Jul 2004.

[46] Peter Karbach and Joachim Stolze. Spin chains as perfect quantum state mirrors. *Phys. Rev. A*, 72:030301, Sep 2005.

[47] T. Shi, Y. Li, Z. Song, and C.-P. Sun. Quantum-state transfer via the ferromagnetic chain in a spatially modulated field. *Phys. Rev. A*, 71(3):032309, Mar. 2005.

[48] G. L. Giorgi and T. Busch. Quantum state transfer in the presence of nonhomogeneous external potentials. *Phys. Rev. A*, 88(6):062309, Dec. 2013.

[49] S. Lorenzo, T. J. G. Apollaro, A. Sindona, and F. Plastina. Quantum-state transfer via resonant tunneling through local-field-induced barriers. *Phys. Rev. A*, 87(4):042313, Apr. 2013.

[50] C. E. Shannon. A mathematical theory of communication. *The Bell System Technical Journal*, 27(3):379–423, 1948.

[51] Benjamin Schumacher. Quantum coding. *Phys. Rev. A*, 51:2738–2747, Apr 1995.

[52] Richard P. Feynman. *The Feynman Lectures on Physics*. Addison-Wesley Pub. Co., Reading, Mass., 1963–1965.

[53] P.A.M. Dirac. *The Principles of Quantum Mechanics*. Comparative Pathobiology - Studies in the Postmodern Theory of Education. Clarendon Press, 1981.

[54] Michael A. Nielsen and Isaac L. Chuang. *Quantum Computation and Quantum Information: 10th Anniversary Edition*. Cambridge University Press, 2010.

[55] Benjamin Schumacher and Michael Westmoreland. *Quantum Processes, Systems, and Information*. Cambridge University Press, 2010.

[56] R. Shankar. *Principles of Quantum Mechanics*. Springer New York, NY, second edition, 1994.

[57] Wojciech Hubert Zurek. Decoherence, einselection, and the quantum origins of the classical. *Reviews of Modern Physics*, 75(3):715–775, May 2003.

[58] Claus Kiefer and Erich Joos. *Decoherence: Concepts and examples.* Springer Berlin Heidelberg, 1998.

[59] Erich Joos, H. Dieter Zeh, Claus Kiefer, Domenico Giulini, Joachim Kupsch, and Ion-Olimpiu Stamatescu. *Decoherence and the Appearance of a Classical World in Quantum Theory.* Springer-Verlag Berlin Heidelberg, 2 edition, 2003. Originally published under Giulini, D.J.W.

[60] Maximilian Schlosshauer. The quantum-to-classical transition and decoherence, 2019. In: arXiv:quant-ph/1404.2635.

[61] Heinz-Peter Breuer and Francesco Petruccione. *The Theory of Open Quantum Systems.* Oxford University Press, 01 2007.

[62] Austin G. Fowler, Matteo Mariantoni, John M. Martinis, and Andrew N. Cleland. Surface codes: Towards practical large-scale quantum computation. *Physical Review A*, 86(3), September 2012.

[63] Craig Gidney and Martin Ekerå. How to factor 2048 bit RSA integers in 8 hours using 20 million noisy qubits. *Quantum*, 5:433, April 2021.

[64] Ze-Liang Xiang, Sahel Ashhab, J. Q. You, and Franco Nori. Hybrid quantum circuits: Superconducting circuits interacting with other quantum systems. *Rev. Mod. Phys.*, 85:623–653, Apr 2013.

[65] Tycho Sleator and Harald Weinfurter. Realizable universal quantum logic gates. *Phys. Rev. Lett.*, 74:4087–4090, May 1995.

[66] Seth Lloyd. Almost any quantum logic gate is universal. *Phys. Rev. Lett.*, 75:346–349, Jul 1995.

[67] J. I. Cirac and P. Zoller. Quantum computations with cold trapped ions. *Phys. Rev. Lett.*, 74:4091–4094, May 1995.

[68] J. R. Petta, A. C. Johnson, J. M. Taylor, E. A. Laird, A. Yacoby, M. D. Lukin, C. M. Marcus, M. P. Hanson, and A. C. Gossard. Coherent manipulation of coupled electron spins in semiconductor quantum dots. *Science*, 309(5744):2180–2184, 2005.

[69] Charles Bennett and David DiVincenzo. Quantum information and computation. *Nature*, 404(6775):247–255, 2000.

[70] Luc Vinet and Alexei Zhedanov. How to construct spin chains with perfect state transfer. *Phys. Rev. A*, 85:012323, Jan 2012.

[71] C. Albanese, M. Christandl, N. Datta, and A. Ekert. Mirror inversion of quantum states in linear registers. *Phys. Rev. Lett.*, 93:230502, 2004.

[72] Chris Godsil. State transfer on graphs. *Discrete Mathematics*, 312(1):129–147, 2012. Algebraic Graph Theory — A Volume Dedicated to Gert Sabidussi on the Occasion of His 80th Birthday.

[73] C. M. van Bommel. Pretty good state transfer of multiple qubit states on paths. *Quantum Information and Computation*, 19(7 & 8):361–376, Jun 2019.

[74] W. Heisenberg. Zur theorie des ferromagnetismus. *Zeitschrift für Physik*, 49:619–636, 1928.

[75] Thierry Giamarchi. *Quantum Physics in One Dimension.* Oxford University Press, 12 2003.

[76] Henrik Bruus and Karsten Flensberg. *Many-body quantum theory in condensed matter physics - an introduction.* 2004.

[77] Michael P. Marder. *Condensed Matter Physics.* John Wiley & Sons, Inc., Hoboken, New Jersey, 2010.

[78] P. Jordan and E. Wigner. Über das paulische Äquivalenzverbot. *Zeitschrift für Physik*, 47:631–651, 1928.

[79] Oleg Derzhko. Jordan-wigner fermionization for spin-1/2 systems in two dimensions: A brief review, 2001. In: arXiv:cond-mat/0101188.

[80] Charles Kittel and Donald F. Holcomb. Introduction to Solid State Physics. *American Journal of Physics*, 35(6):547–548, 06 1967.

[81] B. Paredes, A. Widera, V. Murg, et al. Tonks–girardeau gas of ultracold atoms in an optical lattice. *Nature*, 429:277–281, 2004.

[82] Irene D'Amico. Quantum dot-based quantum buses for quantum computer hardware architecture. *Microelectronics Journal*, 37(12):1440–1441, 2006.

[83] X.-L. Deng, D. Porras, and J. I. Cirac. Effective spin quantum phases in systems of trapped ions. *Phys. Rev. A*, 72:063407, Dec 2005.

[84] X. Li, Y. Ma, J. Han, Tao Chen, Y. Xu, W. Cai, H. Wang, Y.P. Song, Zheng-Yuan Xue, Zhang-qi Yin, and Luyan Sun. Perfect quantum state transfer in a superconducting qubit chain with parametrically tunable couplings. *Phys. Rev. Appl.*, 10:054009, Nov 2018.

[85] Christof Weitenberg, Manuel Endres, Jacob F. Sherson, Marc Cheneau, Peter Schauß, Takeshi Fukuhara, Immanuel Bloch, and Stefan Kuhr. Single-spin addressing in an atomic mott insulator. *Nature*, 471(7338):319–324, March 2011.

[86] C. J. van Diepen, T.-K. Hsiao, U. Mukhopadhyay, C. Reichl, W. Wegscheider, and L. M. K. Vandersypen. Quantum simulation of antiferromagnetic heisenberg chain with gate-defined quantum dots. *Phys. Rev. X*, 11:041025, Nov 2021.

[87] Dylan Lewis, Leonardo Banchi, Yi Hong Teoh, Rajibul Islam, and Sougato Bose. Ion trap long-range xy model for quantum state transfer and optimal spatial search. *Quantum Science and Technology*, 8(3):035025, June 2023.

[88] Michał Horodecki, Paweł Horodecki, and Ryszard Horodecki. General teleportation channel, singlet fraction, and quasidistillation. *Phys. Rev. A*, 60(3):1888–1898, 1999.

[89] Alastair Kay. Perfect, efficient, state transfer and its application as a constructive tool. *International Journal of Quantum Information*, 08(04):641–676, June 2010.

[90] Man-Hong Yung. Quantum speed limit for perfect state transfer in one dimension. *Phys. Rev. A*, 74:030303, Sep 2006.

[91] Abdulfateh Bezaz. Perfect state transfer in spin-chains with on-site energy parametrization. 2023.

[92] Fateh Bezaz, Chad C. Nelmes, Irene D'Amico, and Timothy Spiller. Quasi-perfect state transfer in spin chains via the parametrization of the on-site energies. Preprint to be submitted to *Physica Scripta*, 2024.

[93] Luke Mortimer, Marta P. Estarellas, Timothy P. Spiller, and Irene D'Amico. Evolutionary computation for adaptive quantum device design. *Advanced Quantum Technologies*, 4(8):2100013, 2021.

[94] Francisco Domínguez-Serna and Fernando Rojas. Quantum control using genetic algorithms in quantum communication: superdense coding. *Journal of Physics: Conference Series*, 624(1):012009, Jun 2015.

[95] A. Eiben and J. Smith. From evolutionary computation to the evolution of things. *Nature*, 521:476–482, 2015.

[96] A. Lambora, K. Gupta, and K. Chopra. Genetic algorithm- a literature review. In *2019 International Conference on Machine Learning, Big Data, Cloud and Parallel Computing (COMITCon)*, pages 380–384, 2019.

[97] Ole H. Hald. Inverse eigenvalue problems for jacobi matrices. *Linear Algebra and its Applications*, 14(1):63–85, 1976.

[98] C. de Boor and G.H. Golub. The numerically stable reconstruction of a jacobi matrix from spectral data. *Linear Algebra and its Applications*, 21(3):245–260, 1978.

[99] H. Hochstadt. On the construction of a jacobi matrix from mixed given data. *Linear Algebra and its Applications*, 28:113–115, 1979.

[100] B. N. Parlett. *The Symmetric Eigenvalue Problem*. Classics in Applied Mathematics. Society for Industrial and Applied Mathematics, 1980.

[101] Graham M. L. Gladwell. *Inverse Problems in Vibration*. 1986.

[102] Chris Godsil, Stephen Kirkland, Simone Severini, and Jamie Smith. Number-theoretic nature of communication in quantum spin systems. *Phys. Rev. Lett.*, 109:050502, Aug 2012.

[103] A Cacheffo, M A de Ponte, M H Y Moussa, and A S M de Castro. Quasi-perfect state transfer in a bosonic dissipative network. *Journal of Physics B: Atomic, Molecular and Optical Physics*, 43(10):105503, 2010.

[104] Scott Aaronson. *Quantum Computing since Democritus*. Cambridge University Press, 2013.

[105] Abdulsalam H. Alsulami, Irene D'Amico, Marta P. Estarellas, and Timothy P. Spiller. Scalable quantum spin networks from unitary construction. *Advanced Quantum Technologies*, 7(2):2300238, 2023.